Anti-disturbance performance analysis and the innovative design of the FAST fine-tuning platform

Jinhao Duan, Hanqing Liu, Zhufeng Shao, Rui Yao, Zhaokun Zhang, Stéphane Caro

Anti-disturbance performance analysis and the innovative design of the FAST fine-tuning platform

Jinhao Duan [a,b], Hanqing Liu [a,b] , Zhufeng Shao [a,b,*] , Rui Yao [c] , Zhaokun Zhang [d], Stéphane Caro[e]

[a] *State Key Laboratory of Tribology & Institute of Manufacturing Engineering, Department of Mechanical Engineering, Tsinghua University, Beijing 100084, China*
[b] *Beijing Key Lab of Precision/Ultra-precision Manufacturing Equipments and Control, Tsinghua University, Beijing 100084, China*
[c] *CAS Key Laboratory of FAST, National Astronomical Observatories, Chinese Academy of Sciences, Beijing 100101, China*
[d] *Peng Cheng Laboratory, Shenzhen 518055, China*
[e] *Lab. des Sci. du Numerique de Nantes, Nantes, France*

Abstract: In order to further increase the observation range and sensitivity of the Five-hundred-meter Aperture Spherical Telescope (FAST), an innovative design of the cable-driven fine-tuning platform (CDFP) is required to replace the existing bulky rigid mechanism to increase rotation capability and reduce weight for more powerful receivers. A key issue is to ensure its stability and anti-disturbance ability. In this paper, an intuitive illustration and analysis method is proposed on the anti-disturbance ability of cable-driven parallel robots (CDPRs), based on the Available Wrench Set (AWS). The approach decomposes the high-dimensional wrench space into the low-dimensional force space and the moment space, enabling the visualized analysis of the anti-disturbance performance and avoiding dimensional inconsistency. On this basis, auxiliary branches are introduced to enhance the anti-disturbance ability of CDPR. Anti-disturbance performance of the CDFP is analyzed, and simulation indicates that the anti-disturbance performance of the CDFP is improved by 186%, and will greatly improve the observation capabilities of the FAST. This paper provides an efficient method for analyzing and improving the anti-disturbance ability of the CDPR.

Keywords: Anti-disturbance performance, Design, Cable-driven parallel robot, Auxiliary branches

1. Introduction

The Five-hundred-meter Aperture Spherical Telescope (FAST) is the largest single-aperture radio telescope in the world with the highest sensitivity and the best comprehensive performance [1,2]. The feed support system [3] realizes the motion of the feed cabin of FAST, and consists of two levels. As is shown in Fig. 1(a), the first level is a cable-driven parallel robot (CDPR) with six cables, which realizes motion and attitude adjustment of the feed cabin, which is referred to as the first-level cable platform. As is shown in Fig. 1(b) and (c), the second level consists of the A-B rotator and the Gough-Stewart parallel mechanism located in the feed cabin, which is referred to as the fine-tuning platform. The A-B rotator is used to increase the range of the zenith angle, which is the angle between the incident signal and the local zenith direction. And the Gough-Stewart parallel mechanism is used to compensate for terminal tracking errors. The receivers are installed on the end effector of the Gough-Stewart parallel mechanism. To cope with the increasing observation requirement, the FAST needs to have better observation range and sensitivity. A new receiver is ready for installation, which is more sensitive but heavier. Designing a new fine-tuning platform with lightweight, high load, and large pitch angle is desperately needed.

The CDPR inherits the advantages of cable-driven technology and parallel mechanism [4], such as lightweight, cost-effective, high load, and extensive workspace, which has been applied in fields of large equipment maintenance [5,6], warehousing logistics [7,8], construction [9,10], and motion simulation [11]. CDPR provides a feasible approach for the new fine-tuning platform. However, challenges exist in the anti-disturbance performance with large pitch angle, which includes two aspects: the ability to resist external forces (anti-force performance) and the ability to resist external moments (anti-moment performance).

CDPRs are primarily classified into two categories as shown in Fig. 2. One category relies on the force due to gravity to tension cables, known as suspended CDPRs or CSPRs (Cable-Suspended Parallel Robot). Examples include FAST [1], RoboCrane [12], CoGiRo [13], etc. The suspended CDPR has limited capabilities in exerting forces and moments. The other category tension the cables by pulling each other from both sides of the end effector as the tensegrity. Examples include CABLAR [8], CableRobot [14], Hephaestus [15], etc. This type of CDPR can generate high acceleration and large forces. However, this category of CDPR requires more cables than suspended CDPR with the same DOFs (degrees of freedom) because cables should be arranged on both sides of the end effector, leading to complex control, higher energy consumption, and a larger framework. The CDPRs could be equipped with rigid branches to simplify the configuration and improve the performances of acceleration and anti-disturbance, avoiding redundant actuation [16]. BetaBot [17] and TBot [18,19] utilize the cylinder or spring branches to effectively improve the acceleration ability and workspace. The suspended CDPRs meet the lightweight and large rotation requirements of the fine-tuning platform. Auxiliary branches can be added to enhance the anti-disturbance performance [20,21].

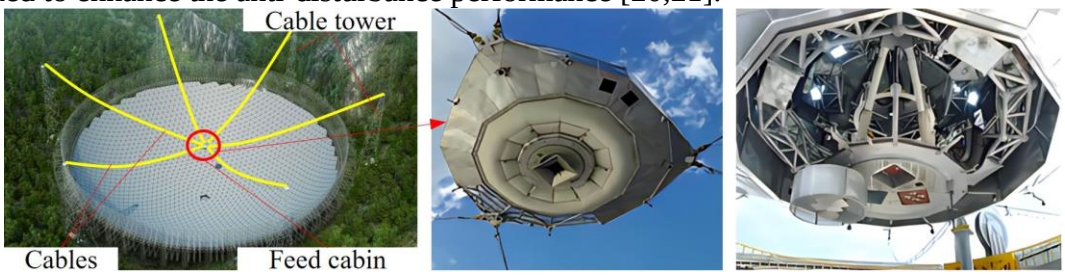

(a) Cable-driven parallel robot (b) Feed cabin (c) Fine-tuning platform

Figure 1: The feed support system of FAST

(a) CoGiRo (Category I) (b) Hephaestus (Category II) (c) TBot (Auxiliary branch)

Figure 2: Typical CDPRs

The anti-disturbance ability of the CDPR means the end effector can maintain stationary or uniform motion when subjected to external forces, without slack or overload of cables [22,23]. Representing the force output and anti-disturbance ability of robots as polyhedron is a good representation method. Finotello et al. [24] pointed out the possibility of using polyhedrons to analyze the velocity and force output performance of robots. Garg et al. [25] and Zibil et al. [26] utilized polyhedrons to analyze the wrench capability of rigid parallel robots. Around the same time, Bosscher et al. [27] applied the polyhedron method to the analysis of CDPR, considering the fact that cables can only transmit tension but not pressure, which is different from rigid parallel robots. Then, Bouchard et al. [28] provided a clear definition and two methods to determine the Available Wrench Set (AWS) based on the previous research. Task Wrench Set (TWS) or Required Wrench Set (RWS) is proposed to represent the set of required wrenches to achieve the task [29]. And positional relationship between AWS and TWS in wrench space is used to determine the reachability of poses [20]. AWS has been applied to analyze and improve the anti-disturbance performance. Liu et al. [22] investigated the force output performance of the translational CDPR with the AWS in force space. Springs are used to shift the current force state point toward the center of the AWS [30]. Sun et al. [31] increased the volume of the AWS by adding thrusters to the CDPR end effector. Chan et al. [32] introduced the torque-speed relationship into the analysis of anti-disturbance performance. These studies simplify the end effector as a point, and the external moment is rarely discussed. When analyzing the anti-disturbance performance of CDPRs with more than three DOFs or CDPRs with both translational and rotational DOFs, the AWS becomes a polyhedron beyond 3D space that is hard to express intuitively and has the problem of dimensional

inconsistency. As a result, the analysis and optimization of anti-disturbance ability become abstract and difficult.

In this paper, a novel analysis method of the anti-disturbance performance is proposed, and a method to improve the anti-disturbance ability with auxiliary branches is established. A new cable-driven fine-tuning platform (CDFP) of the FAST is designed and meets the requirements of increasing the zenith angle and achieving lightweight. Anti-disturbance performance of the CDFP is analyzed with the proposed methods. Auxiliary branches are equipped and analyzed, and their forces are optimized, enhancing the anti-disturbance performance of the new CDFP. The paper is organized as follows. Section 2 briefly introduces the new CDFP as the research object. In Section 3, the analysis and optimization methods of the anti-disturbance performance are proposed for CDPRs. In Section 4, auxiliary branches are introduced, and the performance of CDFP with zero, one, and three auxiliary branches is analyzed in turn. Section 5 implements the simulation and verification of proposed methods on the new CDFP. Section 6 gives the conclusions.

2. The cable-driven fine-tuning platform (CDFP)

The fine-tuning platform is responsible for realizing the zenith angle based on the orientation of the first-level cable platform and compensating for the terminal error caused by the wind disturbance. The angle description adopts the ZYZ Euler angle. Two variables are used here to determine the orientation, which are the direction angle θ and the pitch angle φ. The orientation of the fine-tuning platform can be expressed as the rotation with the following three steps:

(1) Rotate θ around the Z-axis of the local coordinate system.

(2) Rotate φ around the Y-axis of the generated new local coordinate system in step (1).

(3) Rotate $-\theta$ around the Z-axis of the generated new local coordinate system in step (2).

During the astronomical observation, the terminal position error should be less than Root Mean Square (RMS) 10mm, and the angle error should be less than RMS 1°. The maximum zenith angle of 50° needs to be achieved, and the pitch angle distribution of the two-level feed support system is shown in Eq. (1):

$$\begin{aligned} \varphi_{\text{sta}} &= \begin{cases} \dfrac{3}{8}\varphi_z & 0 \le \varphi_z \le 35° \\ \left(\dfrac{1}{225}\varphi_c - \dfrac{1}{12}\right)\varphi_z^{\,2} + \left(-\dfrac{14}{45}\varphi_c + \dfrac{149}{14}\right)\varphi_z + \left(\dfrac{14}{9}\varphi_c - \dfrac{1225}{12}\right) & 35° \le \varphi_z \le 50° \quad \varphi_c = 14° \end{cases} \\ \varphi_{end} &= \varphi_z - \varphi_{sta} \end{aligned} \tag{1}$$

in which, φ_z is the required pitch angle for the astronomical observation, which is usually called the zenith angle. It is the angle between the Z-axis of the end effector of the fine-tuning platform (Z_{P}) and the Z-axis of the global coordinate system around the Y-axis of the fine-tuning platform (Y_{P}). φ_{sta} is the pitch angle of the first-level cable platform, which is the angle between the Z-axis (Z_{B}) of the end effector of the first-level cable platform and the Z-axis of the global system around the Y-axis of the end effector of the first-level cable platform (Y_{B}). φ_{end} is the pitch angle of the fine-tuning platform, which is the angle between the Z-axis of the fine-tuning platform (Z_{P}) and the Z-axis of the first-level cable platform (Z_{B}) around the Y-axis of the fine-tuning platform (Y_{P}). φ_c is the constant coefficient used to fit the angle distribution into a quadratic equation. The unit of variables φ_{end}, φ_{sta} and φ_z in Eq. (1) is degree (°). The zenith angle, pitch angle, and direction angle are shown in Fig. 3. The pitch angles φ_{end}, φ_{sta} and φ_z can be directly summed or subtracted here because the Y-axis of the fine-tuning platform (Y_{P}) and the Y-axis of the first-level cable platform (Y_{B}) are collinear.

Eq. (1) is a fitted polynomial determined according to the research of the CAS Key Laboratory of FAST [33]. During the observation, the first-level cable platform maintains a certain pitch angle according to its position to ensure balanced cable forces. The maximum value of this pitch angle φ_{sta} is 14°. In addition, the first-level cable platform has a maximum position error of 48mm relative to the ideal position during observation.

Therefore, the motion capabilities that need to be achieved by the fine-tuning platform are:

(1) Pitch angle of 0~36° with direction angle of 0~360°, which collaborates with the first-level cable platform to achieve the maximum zenith angle of 50°

(2) Translational motion of 100mm in all directions, which compensates for the position error of the first-level cable platform.

A 6-cable suspended CDPR is adopted as the new fine-tuning platform, as shown in Fig. 4. Actuation units are installed on the base, which adopts a guide rail, and the slider is equipped with guide pulleys. Cables are retracted and released by the movement of the sliders. The estimated mass of the end effector is 4300kg. Optimization design is carried out to satisfy the constraints and performance requirements. And modeling and parameters of the CDFP are given in the Appendix.

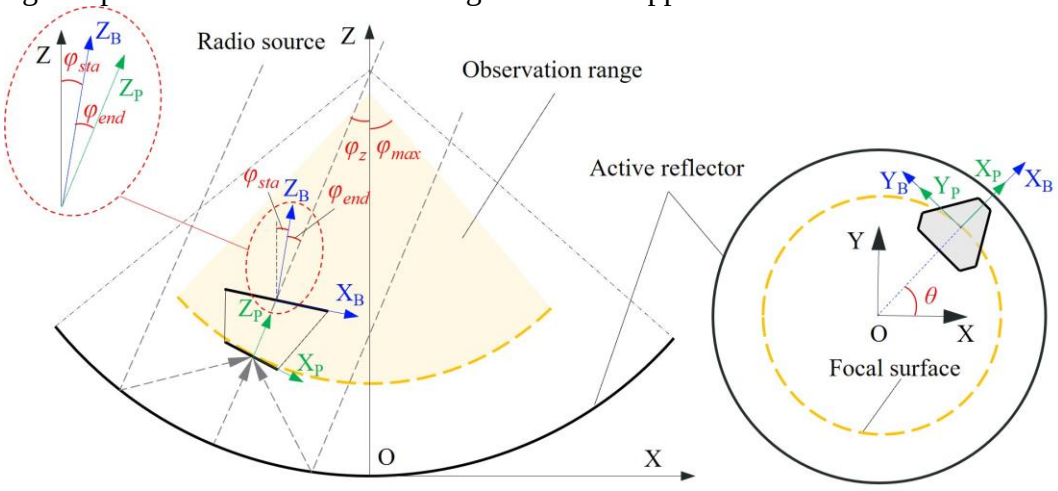

(a) Main view (b) Top view

Figure 3: Zenith angle, pitch angle and direction angle

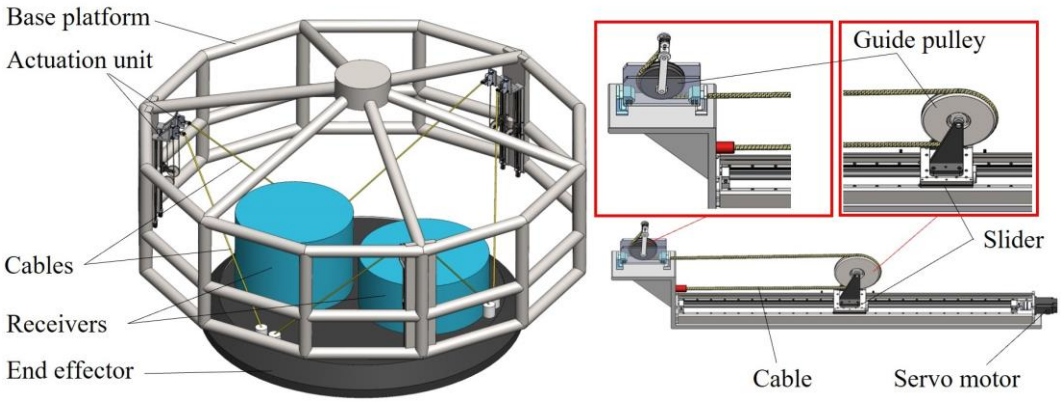

(a) Cable-driven Fine-tuning platform (b) Actuation unit

Figure 4: The structure of CDFP

3. Analysis method of the anti-disturbance performance

Since the rigid A-B rotator and Gough-Stewart parallel mechanism are replaced with the CDFP, the anti-disturbance ability needs to be analyzed to ensure the reliability and stability of the FAST feed support system. In this Section, we introduce the construction methods of the AWS [28]. And the steps to decompose the AWS into polyhedrons separately in the force and moment spaces are proposed, which are force convex hull and moment convex hull. A planar 3-DOF CDPR is taken as an example to clearly illustrate the decomposition process. Finally, the strategy to improve the anti-disturbance performance is proposed with the auxiliary branch.

3.1 The AWS

In practice, the CDPR may be subject to various external disturbances, and the anti-disturbance performance needs to be analyzed. The AWS of the CDPR with m cables can be expressed at the given pose as:

$$
\begin{aligned}
&\mathrm{AWS}=\left\{\boldsymbol{x}\in \mathrm{R}^{d} \mid \boldsymbol{x}=\sum_{i=1}^{n} t_i\begin{bmatrix}\boldsymbol{e}_i\\ \boldsymbol{u}_i\end{bmatrix},\ \underline{t_i}\le t_i\le \overline{t_i}\right\}=\left\{\boldsymbol{x}\in \mathrm{R}^{d} \mid \boldsymbol{x}=\boldsymbol{J}diag(\boldsymbol{\Delta t})\boldsymbol{\alpha}+\boldsymbol{J}^{T}\underline{\boldsymbol{t}}\right\}\\
&\boldsymbol{\Delta t}=[\Delta t_1\ \ \cdots\ \ \Delta t_m]^{T},\ \Delta t_i=\overline{t_i}-\underline{t_i},\ \underline{\boldsymbol{t}}=[\underline{t_1}\ \ \cdots\ \ \underline{t_m}]^{T}\\
&\boldsymbol{\alpha}=[\alpha_1\ \ \cdots\ \ \alpha_m]^{T},\ 0\le\alpha_i\le 1,\ \boldsymbol{J}=\begin{bmatrix}\boldsymbol{e}_1 & \ldots & \boldsymbol{e}_m\\ \boldsymbol{u}_1 & \ldots & \boldsymbol{u}_m\end{bmatrix}^{T},i=1,2,...,m
\end{aligned}
\tag{2}
$$

where, t_i is the tension of the i^{th} cable, $\underline{t_i}$ and $\overline{t_i}$ are the minimum and maximum tension constraints of the i^{th} cable, $\boldsymbol{J}$ is the Jacobian matrix of the CDPR, $\boldsymbol{e}_i$ is the unit direction vector of the i^{th} cable, and $\boldsymbol{u}_i$ is the unit rotation vector of the i^{th} cable.

The AWS is the set of the tension vector sum that the cables can produce and exert to the end effector. Geometrically, the wrenches that a single cable can exert to the end effector is a line segment in the wrench space. Perform the Minkowski sum operation on all the line segments in the wrench space, and the deduced polyhedron is the AWS [28,29].

The points in the wrench space are represented with the bold italic capital letter with a hat above it. The external wrench can be expressed as the wrench state point $\hat{\boldsymbol{Q}}_e$. If the point $\hat{\boldsymbol{Q}}_e$ is inside the AWS, the end effector can maintain stability. The distance from $\hat{\boldsymbol{Q}}_e$ to the AWS boundary in a direction represents the margin for the end effector to withstand the external wrench in this direction. If the point $\hat{\boldsymbol{Q}}_e$ is outside the AWS, the end effector will lose control. The AWS is represented in an *n*-dimensional wrench space, and has two methods to deduce, namely the convex hull method and the hyperplane shifting method [28,34,35].

For the convex hull method, a set of vertices is obtained by arranging, combining, and summing the maximum and minimum tensions that each cable can provide. The AWS is obtained by solving the convex hull of the vertex set. For an *n*-DOF CDPR with *m* cables, the number of combinations of maximum and minimum cable tensions is $k=2^m$. The coordinates of each tension combination in the wrench space correspond to a node $\hat{\boldsymbol{N}}_i$, and $\{\hat{\boldsymbol{N}}\}=\{\hat{\boldsymbol{N}}_1\ \ \ldots\ \ \hat{\boldsymbol{N}}_k\}$ is the set of nodes that contains all combinations. It should be noted that we only discuss the fully constrained CDPR in this research, in which $n\le m-1$. And when analyzing the suspended CDPRs that rely on the gravity force to tension the cables, $n\le m$.

Further, $\{\hat{\boldsymbol{P}}\}=\{\hat{\boldsymbol{P}}_1\ \ \ldots\ \ \hat{\boldsymbol{P}}_s\}$ is the set of vertices obtained by performing a convex hull operation on the node-set $\{\hat{\boldsymbol{N}}\}$. The element $\hat{\boldsymbol{P}}_i$ in $\{\hat{\boldsymbol{P}}\}$ corresponds to the node in the set $\{\hat{\boldsymbol{N}}\}$ that falls at the vertex of the convex polyhedron obtained by solving the convex hull, in which $\{\hat{\boldsymbol{P}}\}\subseteq\{\hat{\boldsymbol{N}}\}$ and $s\le k$. The equal sign holds when the CDPR is non-redundant and the pose is nonsingular [28]. The solution of the convex hull method is the set of vertices $\{\hat{\boldsymbol{P}}\}$ and can be expressed as:

$$
\begin{aligned}
&\mathrm{AWS}=conv\left\{\hat{\boldsymbol{N}}\right\}=conv\left\{\hat{\boldsymbol{P}}\right\}\\
&\{\hat{\boldsymbol{N}}\}=\{\hat{\boldsymbol{N}}_1\ \ \ldots\ \ \hat{\boldsymbol{N}}_k\}=\left\{\boldsymbol{x}\in \mathrm{R}^{n} \mid \boldsymbol{x}=\boldsymbol{J}diag(\boldsymbol{\Delta t})\boldsymbol{\alpha}+\boldsymbol{J}^{T}\underline{\boldsymbol{t}}\ \right\},\ \boldsymbol{\alpha}=[\alpha_1\ \ \cdots\ \ \alpha_k]^{T},\ \alpha_i=\{0,1\}
\end{aligned}
\tag{3}
$$

where *conv* represents solving the convex hull. The number of vertices is up to $\sum_{i=0}^{m} C_m^i$. The advantage of the convex hull method is that it easily and intuitively obtains all vertices, and is convenient to draw the AWS in the wrench space with the existing function libraries like Qhull [36], in which vertices are common-used inputs of these functions. By observing the position of the wrench state point and the AWS, we can intuitively evaluate the anti-disturbance performance and analyze the approach to improve it. The disadvantage is that the number of vertices increases significantly with the cable number and the computational complexity of solving the convex hull surges. For the most commonly used Quickhull algorithm [36], when the dimension is not larger than three, the computational complexity is $O(n\log v)$. When the dimension is larger than three, the computational complexity is $O(n^{d-1}\log n)$ [37]. In which, *n* is the number of input points, *v* is the number of output points, and *d* is the number of dimensions.

The hyperplane shifting method represents the AWS as the intersection of a series of half-spaces.

Each half-space can be described by an inequality:

$$\boldsymbol{w}_i^T \boldsymbol{x} - b_i \le 0 \tag{4}$$

where $\boldsymbol{w}_i$ is the normal vector of the hyperplane α_i that splits the wrench space into two half-spaces. b_i is the intercept of the hyperplane. The hyperplane α_i can be expressed by the equation $\boldsymbol{w}_i^T \boldsymbol{x} - b_i = 0$. The inequality system that determines AWS can be organized into the following form:

$$AWS = \left\{ \boldsymbol{x} \in \mathrm{R}^n \mid \boldsymbol{W}^T \boldsymbol{x} - \boldsymbol{b} \le 0 \right\} \tag{5}$$

where $\boldsymbol{W} = [\boldsymbol{w}_1 \quad \dots \quad \boldsymbol{w}_k]$ are the normal vectors of all the hyperplanes. $\boldsymbol{b} = [b_1 \quad \dots \quad b_k]^T$ is intercepts of all the hyperplanes. Since each cable contains the tension constraint, the normal vectors in $\boldsymbol{W}$ are paired, and $\boldsymbol{w}_i = -\boldsymbol{w}_{i+k/2}$ for $i = 1,\dots,k/2$. For a *n*-DOF CDPR with *m* cables, the hyperplane number is up to $k = 2C_m^{n-1}$. C_m^i represents the combination of i and m, and $C_m^i = m!/i!(m-i)!$. It should be noted that for each row of the inequalities, $d_i = (\boldsymbol{w}_i^T \boldsymbol{x} - b_i) / \|\boldsymbol{w}_i\|$ represents the distance between the wrench state $\boldsymbol{x}$ and the hyperplane corresponding to the i^{th} inequality $\boldsymbol{w}_i^T \boldsymbol{x} - b_i \le 0$. The advantage of the hyperplane shifting method is that for CDPRs with a large cable number, the solving efficiency is much higher than the convex hull method. For a *n*-DOF CDPR with *m* cables (*n*>3), there will be 2^m nodes when using the convex hull method, and the computational complexity of the convex hull is $O(2^{m(n-1)} \log 2^m)$. When using the hyperplane shifting method, the number of hyperplanes is only $2C_m^{n-1}$, and the number of inequalities is also only $2C_m^{n-1}$. And it is easy to judge whether $\hat{\boldsymbol{Q}}_e$ is in the AWS with the inequalities, avoiding complicated convex hull operations. The disadvantage is that it is difficult to directly plot the polyhedron with existing libraries, and the existing library files are limited. A lot of algorithm development work is required. And the region enclosed by hyperplanes is not as intuitive as a polyhedron constructed based on vertices.

Take a planar 3-cable CSPR as an example. As shown in Fig. 5(a), the CSPR has two translational DOFs along the X-axis and the Z-axis, and has a rotational DOF around the Y-axis. The gravity is along the negative direction of the Z-axis. And $\boldsymbol{G}$ is the force due to gravity. Its wrench space is a 3-dimensional space containing two force dimensions and one moment dimension. As is shown in Fig. 5(b) and (c), when using the convex hull method, the AWS of the CSPR is a parallelepiped with $\{\hat{\boldsymbol{P}}\} = \{\hat{\boldsymbol{P}}_1 \quad \dots \quad \hat{\boldsymbol{P}}_8\}$ as the set of vertices. For the hyperplane shifting method, the AWS is a parallelepiped enclosed by hyperplanes $\alpha_1 \sim \alpha_6$. The normal vectors $\boldsymbol{W} = [\boldsymbol{w}_1 \quad \dots \quad \boldsymbol{w}_6]$ and the intercepts $\boldsymbol{b} = [b_1 \quad \dots \quad b_6]^T$ of the hyperplanes can be obtained. The AWS obtained by the two methods is equivalent.

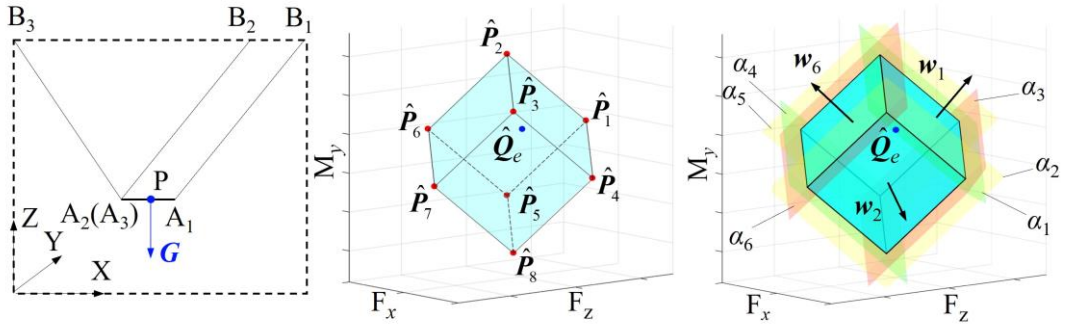

(a) Configuration of the planar 3-cable CSPR

(b) AWS constructed using convex hull method

(c) AWS constructed using hyperplane shifting method

Figure 5: Two methods to represent the AWS.

When the center of mass of the end-effector coincides with the geometric center, the point $\hat{\boldsymbol{Q}}_e$ corresponds to the force due to gravity ($\boldsymbol{G}$) here, which is along the Z-axis. And The coordinate value of $\hat{\boldsymbol{Q}}_e$ on the M_y-axis in the wrench space is zero. When the center of mass of the end-effector does not coincide with the geometric center, the point $\hat{\boldsymbol{Q}}_e$ corresponds to the force due to gravity ($\boldsymbol{G}$) and the moment caused by the gravity ($\boldsymbol{p}_g \times \boldsymbol{G}$) here. In which, $\boldsymbol{p}_g$ refers to the vector from the geometric center of the end-effector to the center of mass of it. And the coordinate value of $\hat{\boldsymbol{Q}}_e$ on the M_y-axis in the

wrench space is $\|\boldsymbol{p}_g \times \boldsymbol{G}\|$, in which $\|\cdot\|$ represents 2-norm.

For the spatial CDPR with more than three DOFs, the dimension of the wrench space is over three. The AWS of these CDPRs is difficult to visualize with images. For CDPR with a non-point end effector, the wrench space contains both force and moment dimensions, and dimensional inconsistencies should be considered during analysis. The FAST CDFP has six cables and six DOFs, and its AWS is a 6-dimensional polyhedron with 64 vertices and 12 faces in the 6-dimensional wrench space, which faces problems of inability to express intuitively and inconsistent dimensions.

Rasheed et al. [20] pointed out the possibility of separately analyzing the anti-force performance and anti-moment performance of CDPRs with hybrid DOFs in the corresponding force and moment spaces. However, the specific solution method and in-depth analysis are not given. In this paper, a novel analysis method of anti-disturbance performance for CDPRs with hybrid DOFs in the high-dimensional wrench space is proposed. By taking the cross-sections at the wrench state point, the AWS in high-dimensional wrench space is decomposed into a force convex hull and a moment convex hull with dimensions no more than three. And the anti-force performance and anti-moment performance can be analyzed intuitively and separately.

Two decomposition methods are proposed. Method I is based on the convex hull method, which can visually express the anti-disturbance performance. Method II is based on the hyperplane shifting method, which has higher solving efficiency.

3.2 AWS decomposition method I

With the convex hull method, the vertices set $\{\hat{\boldsymbol{P}}\} = \{\hat{\boldsymbol{P}}_1 \quad ... \quad \hat{\boldsymbol{P}}_n\}$ of the AWS is deduced, and $\hat{\boldsymbol{P}}_i$ is a vertex of the AWS. Face set $\{\tilde{\boldsymbol{A}}\} = \{\tilde{\boldsymbol{A}}_1 \quad ... \quad \tilde{\boldsymbol{A}}_u\}$ can be obtained with the Qhull library [36]. The vertex orders of all faces of the AWS form a set $\{\underset{\sim}{\boldsymbol{A}}\} = \{\underset{\sim}{\boldsymbol{A}}_1 \quad ... \quad \underset{\sim}{\boldsymbol{A}}_u\}$. $\tilde{\boldsymbol{A}}_i$ represents the i^{th} face of the AWS, $\underset{\sim}{\boldsymbol{A}}_i = \{\underset{\sim}{a}_{i1} \quad ... \quad \underset{\sim}{a}_{iw}\}$ represents the order number of vertices in the vertex set $\{\hat{\boldsymbol{P}}\}$ that determines the i^{th} face $\tilde{\boldsymbol{A}}_i$, and w is the vertex number of $\tilde{\boldsymbol{A}}_i$.

Decomposing the AWS into force/moment convex hulls is a process that solves the intersection of the AWS with the force/moment space. AWS is the Minkowski Sum of a series of line-segments in the wrench space, which is a convex polyhedron. According to the properties of convex hulls, the intersection of two convex hulls is still convex. And the hyperplane is convex. Therefore, the intersection (cross-section) obtained in each step is convex, which is the intersection of a convex polyhedron and a hyperplane [38].

The faces of AWS and the cross-sections of AWS may not necessarily be polygons or polyhedrons with the same number of vertices and edges. For example, the shape of the cross-section of a 4-dimensional hypercube and a hyperplane can be a prism, cuboid, frustum, tetrahedron, etc. The faces of those cross-sections can be triangles (3 vertices and 3 edges), quadrilaterals (4 vertices and 4 edges), and polygons with more vertices and edges. Researchers need to deal with different kinds of polygons with different numbers of vertices when analyzing and programming. To solve this problem, we divide the faces into simplexes. Then, the problem of finding the intersection points between a face with an uncertain number of edges and the hyperplane can be standardized into a series of problems of finding the intersection points between a simplex with a certain number of edges and the hyperplane. The division of the faces into simplexes can be achieved using existing libraries like Qhull.

Simplex is a generalization of a triangle or a tetrahedron, it is the simplest partition of the geometry. A (n-1)-dimensional simplex is a convex polyhedron containing n vertices, and its boundary consists of (n-2)-dimensional simplexes. When an n-dimensional simplex is partitioned into two parts, the simplest convex polyhedron obtained is still an n-dimensional simplex, and the cross-section is a (n-1)-dimensional simplex [40].

A step-by-step method to solve the intersection is used here because it is difficult to directly find the intersection between AWS and the force/moment space for the AWS constructed by the convex hull method, especially when the dimension of AWS is six and the dimension of force/moment space is three [40]. For a CDPR with six DOFs, the steps to obtain the force convex hull by decomposing the AWS in the 6-dimensional wrench space $\{O - F_x F_y F_z M_x M_y M_z\}$ are as follows.

(1) Construct the AWS with the convex hull method and obtain the vertex set $\{\hat{\boldsymbol{P}}\}=\{\hat{\boldsymbol{P}}_1 \quad ... \quad \hat{\boldsymbol{P}}_k\}$. Determine the wrench state point $\hat{\boldsymbol{Q}}_e=[\hat{\boldsymbol{F}}_e,\hat{\boldsymbol{M}}_e]^T=[f_x,f_y,f_z,\tau_x,\tau_y,\tau_z]^T$ based on the known external force and moment exerted on the end effector.

(2) Determine whether the current wrench state point $\hat{\boldsymbol{Q}}_e$ is located inside AWS. If $\hat{\boldsymbol{Q}}_e$ is not in the AWS, it will also not be in the cross-section of AWS, and there is no need for further analysis. The steps for determination are as follows:

(a) Construct a new convex hull $conv\{\hat{\boldsymbol{P}}_{new}\}$ with existing vertices $\{\hat{\boldsymbol{P}}\}$ of AWS and $\hat{\boldsymbol{Q}}_e$ as:

$$conv\{\hat{\boldsymbol{P}}_{new}\}=conv\{\{\hat{\boldsymbol{P}}\},\hat{\boldsymbol{Q}}_e\}=conv\{\hat{\boldsymbol{P}}_1 \quad ... \quad \hat{\boldsymbol{P}}_n,\hat{\boldsymbol{Q}}_e\} \tag{6}$$

in which, the new convex hull $conv\{\hat{\boldsymbol{P}}_{new}\}$ can be obtained by using existing function libraries. And the result is a new set of vertices $\{\hat{\boldsymbol{P}}_{new}\}$.

(b) Compare vertices in the new vertex set $\{\hat{\boldsymbol{P}}_{new}\}$ and the old vertex set $\{\hat{\boldsymbol{P}}\}$.

(c) If all the vertices are the same, it means that the constructed convex hull $conv\{\hat{\boldsymbol{P}}_{new}\}$ is the same as the original one $conv\{\hat{\boldsymbol{P}}\}$, and $\hat{\boldsymbol{Q}}_e$ is in the AWS. Otherwise, it means that $\hat{\boldsymbol{Q}}_e$ is outside the AWS and becomes a new vertex of the constructed new convex hull.

(3) Adding vector $-[0,0,0,\tau_x,\tau_y,\tau_z]$ to all the vertices of AWS and $\hat{\boldsymbol{Q}}_e$. This step is equal to a translational transformation for the AWS and $\hat{\boldsymbol{Q}}_e$, which does not change the position relationship of them. The purpose of this step is to make that the process of taking cross-section in steps (4)~(6) is on hyperplane $M_x=0$, $M_y=0$ and $M_z=0$, which is convenient for programming.

(4) Find all intersections $\{^5\hat{\boldsymbol{C}}\}=\{^5\hat{\boldsymbol{C}}_1 \quad ... \quad ^5\hat{\boldsymbol{C}}_{k1}\}$ between AWS and the hyperplane $M_x=0$. $M_x=0$ is the hyperplane whose moment component M_x is zero, and is the 5-dimensional subspace $\{O-F_xF_yF_zM_yM_z\}$ in the 6-dimensional wrench space. The left superscript *n*-1 indicates that the element is a point in *n*-1 dimensional space. The subscript *k*1 represents the number of intersections. Use these intersections as vertices and construct a 5-dimensional convex hull in the 5-dimensional space $\{O-F_xF_yF_zM_yM_z\}$. The constructed convex hull is the cross-section of space $\{O-F_xF_yF_zM_yM_z\}$ and the *n*-dimensional AWS.

(5) Find all intersections $\{^4\hat{\boldsymbol{C}}\}=\{^4\hat{\boldsymbol{C}}_1 \quad ... \quad ^4\hat{\boldsymbol{C}}_{k2}\}$ between the convex hull constructed in step (4) and the hyperplane $M_y=0$. Use these intersections as vertices and construct a 4-dimensional convex hull in the 4-dimensional space $\{O-F_xF_yF_zM_z\}$.

(6) Find all intersections $\{^3\hat{\boldsymbol{C}}\}=\{^3\hat{\boldsymbol{C}}_1 \quad ... \quad ^3\hat{\boldsymbol{C}}_{k3}\}$ between the convex hull constructed in step (5) and the hyperplane $M_z=0$. Use these intersections as vertices and construct a 3-dimensional convex hull in the 3-dimensional space $\{O-F_xF_yF_z\}$. The constructed new convex hull is the cross-section of the AWS and the force space $\{O-F_xF_yF_z\}$, defined as the force convex hull.

The force convex hull only includes the force dimension. The force state point $\hat{\boldsymbol{F}}_e=[f_x,f_y,f_z]^T$ in the force space represents the external force on the end effector. The position relationship between point $\hat{\boldsymbol{F}}_e$ and the force convex hull reveals the anti-force performance of the CDPR. If $\hat{\boldsymbol{F}}_e$ is not in the force convex hull, there will be slack or overload on the cables, and the CDPR will lose control. If $\hat{\boldsymbol{F}}_e$ is in the force convex hull, the distance form $\hat{\boldsymbol{F}}_e$ to the boundary of the force convex hull in all directions indicates how much external force the CDPR can resist in this direction.

The steps to construct the moment convex hull are similar. The steps to find all intersections $\{^{n-1}\hat{\boldsymbol{C}}\}=\{^{n-1}\hat{\boldsymbol{C}}_1 \quad ... \quad ^{n-1}\hat{\boldsymbol{C}}_{k1}\}$ of the *n*-dimensional AWS in (*n*-1)-dimensional space $\{O-F_xF_yF_zM_yM_z\}$ in the above steps (4)~(6) are as follows:

(a) Divide all faces of the *n*-dimensional AWS into (*n*-1)-dimensional simplexes, whose vertices are all derived from the AWS vertices.

(b) Take out a simplex and find all pairwise combinations of its vertices, totaling C_n^2 combinations.

(c) Determine whether the two vertices $\hat{\boldsymbol{P}}_i$ and $\hat{\boldsymbol{P}}_j$ in each combination are on the same side of the hyperplane $M_x = 0$. If so, the line-segment connected by them will not have an intersection point with the hyperplane. And there is no need for further analysis. If the two vertices $\hat{\boldsymbol{P}}_i$ and $\hat{\boldsymbol{P}}_j$ are on the different sides of the hyperplane, the intersection point ${}^{n-1}\hat{\boldsymbol{C}}_i$ of the line-segment connected by them and the hyperplane can be solved and stored in the intersection set $\{{}^{n-1}\hat{\boldsymbol{C}}\}$. If any vertex $\hat{\boldsymbol{P}}_i$ falls on the hyperplane, it will also be stored in the intersection set.

(d) Repeat steps (b) and (c) until the intersections of all simplexes are determined. And all intersection points $\{{}^{n-1}\hat{\boldsymbol{C}}\} = \{{}^{n-1}\hat{\boldsymbol{C}}_1 \quad ... \quad {}^{n-1}\hat{\boldsymbol{C}}_{k1}\}$ can be obtained.

(e) Construct the convex hull of the intersection set $\{{}^{n-1}\hat{\boldsymbol{C}}\}$, and the cross-section is obtained.

With the proposed method, the two 3-dimensional spaces that reveal the anti-force performance and anti-moment performance are decomposed from the 6-dimensional wrench space. It facilitates intuitive analysis and evaluates the performances on outputting and resisting forces and moments in all directions.

We will take the planar 3-cable CSPR as an example to demonstrate the proposed decomposition process. As shown in Fig. 6, the AWS of this CSPR is a parallelepiped in the 3-dimensional wrench space $\{O - F_x F_z M_y\}$. To separately analyze the anti-force performance, the moment dimension M_y is decomposed.

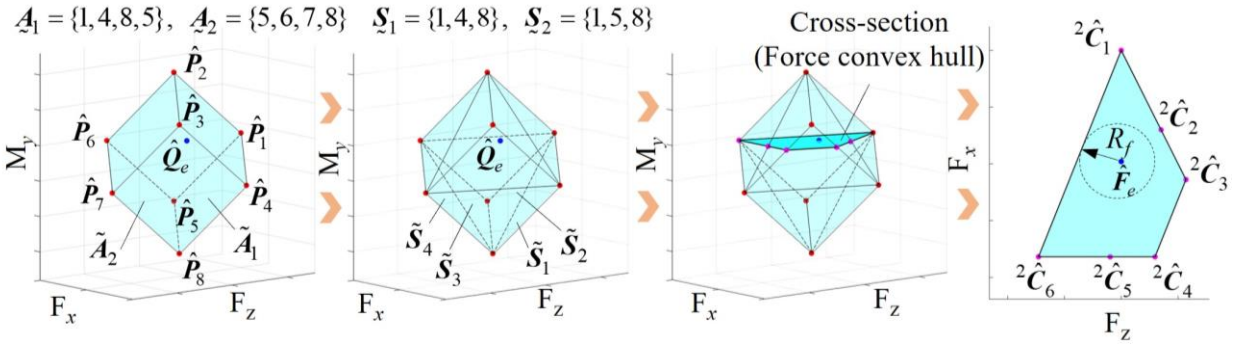

(a) Construct AWS with the vertices

(b) Divide faces into simplexes

(c) Determine intersections and cross-section

(d) Construct the force convex hull

Figure 6: AWS decomposition with the convex hull method

Firstly, move the AWS and wrench state point $\hat{\boldsymbol{Q}}_e = [f_x, f_z, \tau_y]^T$ with the translation vector of $-[0,0,\tau_y]^T$, so that $\hat{\boldsymbol{Q}}_e$ falls on the hyperplane $M_y = 0$. The τ_y of this CSPR is 0 when only subjected to the force due to gravity and does not need translation. As is shown in Fig. 6(a), the AWS has eight vertices $\hat{\boldsymbol{P}}_1 \sim \hat{\boldsymbol{P}}_8$ and six faces $\tilde{\boldsymbol{A}}_1 \sim \tilde{\boldsymbol{A}}_6$. Each face is determined by a set of order number $\tilde{\boldsymbol{A}}_i$. For example, $\tilde{\boldsymbol{A}}_1 = \{1,4,8,5\}$ represents that the face $\tilde{\boldsymbol{A}}_1$ is determined by four vertices $\{\hat{\boldsymbol{P}}_1, \hat{\boldsymbol{P}}_4, \hat{\boldsymbol{P}}_8, \hat{\boldsymbol{P}}_5\}$.

Then, divide all faces into simplexes $\tilde{\boldsymbol{S}}_1 \sim \tilde{\boldsymbol{S}}_{12}$. As shown in Fig. 6(b), each simplex $\boldsymbol{S}_i$ is determined by three vertices and the set of order number is $\tilde{\boldsymbol{S}}_i$. The intersection points of each simplex and the hyperplane $M_y = 0$ are determined in Fig. 6(c), and the intersection set $\{\hat{\boldsymbol{C}}\} = \{{}^2\hat{\boldsymbol{C}}_1 \quad ... \quad {}^2\hat{\boldsymbol{C}}_6\}$ is obtained, which falls in the 2-dimensional force space $\{O - F_x F_z\}$.

Finally, construct the convex hull of the intersection set, and the force convex hull is obtained. As shown in Fig. 6(d), the force convex hull is the convex polygon with intersections $\{{}^2\hat{\boldsymbol{C}}_1, {}^2\hat{\boldsymbol{C}}_3, {}^2\hat{\boldsymbol{C}}_4, {}^2\hat{\boldsymbol{C}}_6\}$ as the vertices.

The force convex hull contains all the force vectors that can be resisted or outputted by the end effector of CSPR. By utilizing the typical geometric features of it, indices can be defined to analyze the typical performance [25,41]. For example, the distance from the wrench state point $\hat{\boldsymbol{Q}}_e$ to the boundary of the force convex hull in each direction shows the ability to resist and output force. The radius R_f of the

inscribed circle centered at $\hat{\boldsymbol{Q}}_e$ represents the anti-force performance in all directions.

It should be noted that the result of the decomposition is the cross-section of AWS and the force space, rather than the projection of AWS on the force space. In addition, the step-by-step approach in steps (4)~(6) are only for the convenience of understanding and programming. Obtaining the cross-section of AWS in the force space can actually be completed in one step, which will be shown in Section 3.3.

3.3 AWS decomposition method II

The AWS constructed by the hyperplane shifting method consists of a series of inequality constraints as $\boldsymbol{W}^T\boldsymbol{x}-\boldsymbol{b}\le 0$. And the force space can be determined by a set of equality constraints. By substituting the equality constraints into the inequality constraints, a new set of inequalities can be obtained, which represents the force convex hull.

Represent the wrench in *n*-dimensional wrench space as $\boldsymbol{x}=[\boldsymbol{x}_F^T \quad \boldsymbol{x}_M^T]^T$. When decomposing the AWS into force space at the wrench state point $\hat{\boldsymbol{Q}}_e$, the equality constraint is $\boldsymbol{x}_M=\hat{\boldsymbol{M}}_e$. The normal vector matrix $\boldsymbol{W}$ can be decomposed into the force sub-matrix $\boldsymbol{W}_F$ and moment sub-matrix $\boldsymbol{W}_M$, in which $\boldsymbol{W}=[\boldsymbol{W}_F^T \quad \boldsymbol{W}_M^T]^T$. Therefore, the inequalities can be written as:

$$\boldsymbol{W}_F^T\boldsymbol{x}_F+\boldsymbol{W}_M^T\boldsymbol{x}_M-\boldsymbol{b}\le 0 \tag{7}$$

Take the moment component $\boldsymbol{x}_M$ as a constant value, the new inequalities obtained are the cross-section of the AWS and force space.

For CDPR with six DOFs, the steps to construct the force convex hull with hyperplane shifting method are as follows:

(1) Construct the AWS with the hyperplane shifting method and obtain the inequalities $\boldsymbol{W}^T\boldsymbol{x}-\boldsymbol{b}\le 0$. Determine the wrench state point $\hat{\boldsymbol{Q}}_e$ based on the external force and moment.

(2) Determine whether the current wrench state point $\hat{\boldsymbol{Q}}_e$ is located inside AWS. The steps are as follows:

(a) Substitute $\hat{\boldsymbol{Q}}_e$ into inequalities obtained in step (1), which can be written as Eq. (8):

$$\boldsymbol{W}^T\hat{\boldsymbol{Q}}_e-\boldsymbol{b}\le 0 \tag{8}$$

(b) If the inequalities are all satisfied, it means that $\hat{\boldsymbol{Q}}_e$ is in the AWS. If the inequalities are not all satisfied, it means that $\hat{\boldsymbol{Q}}_e$ is outside the AWS.

(3) Substitute the moment constraint $\boldsymbol{x}_M=\hat{\boldsymbol{M}}_e$ into the inequalities. The new inequalities are obtained as $\boldsymbol{W}_F^T\boldsymbol{x}_F+\boldsymbol{W}_M^T\hat{\boldsymbol{M}}_e-\boldsymbol{b}\le 0$. Represent constant terms as $\boldsymbol{b}_M=\boldsymbol{b}-\boldsymbol{W}_M^T\hat{\boldsymbol{M}}_e$, the inequalities are generated as $\boldsymbol{W}_F^T\boldsymbol{x}_F-\boldsymbol{b}_M\le 0$, which correspond to the inner of force convex hull. And for each row of the inequalities, $d_i=(\boldsymbol{w}_{Fi}^T\boldsymbol{x}-b_{Mi})/\|\boldsymbol{w}_{Fi}\|$ represents the distance between the force state point $\hat{\boldsymbol{F}}_e$ and the hyperplane corresponding to the i^{th} inequality $\boldsymbol{w}_{Fi}^T\hat{\boldsymbol{F}}_e-b_{Mi}\le 0$ in the force space.

The method to construct the moment convex hull with the hyperplane shifting method is similar. By substituting the force constraint $\boldsymbol{x}_F=\hat{\boldsymbol{F}}_e$ into the inequalities, the inequalities $\boldsymbol{W}_M^T\boldsymbol{x}_M+\boldsymbol{W}_F^T\hat{\boldsymbol{F}}_e-\boldsymbol{b}\le 0$ are obtained, which correspond to the inner of the moment convex hull.

Some faces of the AWS may not directly intersect with the cross-section plane. There are two situations. Situation one occurs when the face does not intersect with the cross-section plane but the hyperplane where the face is located intersects with the cross-section plane. In this situation, the inequality formed will always be satisfied when the other inequalities are satisfied. Situation two occurs when the face is parallel with the cross-section plane. In this situation, the inequality formed will always be satisfied or never be satisfied. Since step (3) is only performed when $\hat{\boldsymbol{Q}}_e$ falls inside the AWS, the new inequality formed will always be satisfied. These situations result in some invalid constraints in the new inequalities, which do not affect the analysis results.

Take the planar 3-cable CSPR as an example. As shown in Fig. 7, the AWS in the 3-dimensional wrench space $\{O-F_xF_zM_y\}$ is determined by the inequalities:

$$\boldsymbol{W}^T\boldsymbol{x}-\boldsymbol{b}\le 0,\boldsymbol{x}\in \mathrm{R}^3,\boldsymbol{W}\in \mathrm{R}^{6\times 3},\boldsymbol{b}\in \mathrm{R}^6 \tag{9}$$

Each row of the inequalities determines a half space in the 3-dimensional wrench space, and α_i is the corresponding hyperplane that divides the space. Finding the cross-section of the AWS in the force space is equivalent to finding the part of the hyperplane β_1 that falls on the area enclosed by hyperplanes $\alpha_1 \sim \alpha_6$, in which the hyperplane β_1 corresponds to the equality constraint $M_y = 0$. And the inequalities become:

$$\boldsymbol{W}_F^{\ T}\boldsymbol{x}_F - \boldsymbol{b} \le 0, \boldsymbol{x}_F \in \mathrm{R}^2, \boldsymbol{W}_F \in \mathrm{R}^{6\times 2}, \boldsymbol{b} \in \mathrm{R}^6 \tag{10}$$

Each row of Eq.10 corresponds to a half space in the 2-dimensional force space $\{O - F_x F_z\}$, and α_i' is the corresponding hyperplane that divides the force space. In the example, α_i' is a line in 2-dimensional force space. α_3' and α_4' are the invalid constraints. $d_i = (\boldsymbol{w}_{Fi}^T \boldsymbol{x} - b_i) / \|\boldsymbol{w}_{Fi}\|$ is the distance from $\hat{\boldsymbol{Q}}_e$ to α_i'.

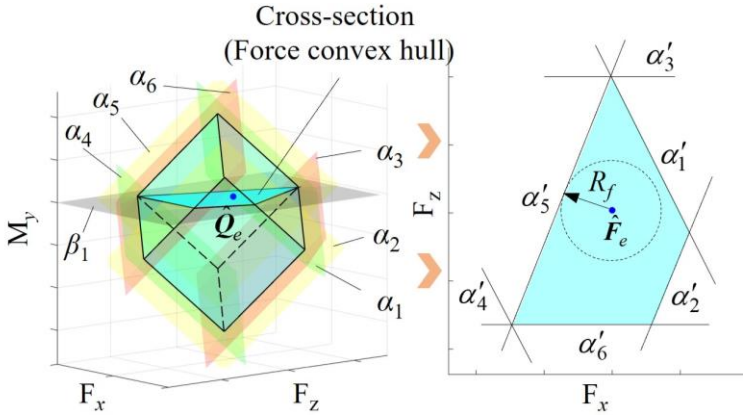

Figure 7: AWS decomposition based on the hyperplane shifting method

Comparatively speaking, method I has the advantage of being intuitive. Decomposed force and moment convex hulls can be obtained and plotted. Analysis and optimization can be carried out intuitively by observing the relationship between the force/moment state point and the convex hull boundary. Method II has the advantage of higher solving efficiency and can solve the anti-disturbance performance quickly.

The radius of the inscribed sphere is an important geometric characteristic of polyhedron. And radius-based indices have been widely used as indices in polyhedron-based performance analysis, such as maximum available value (MAV) and maximum isotropic value (MIV) [41]. To quantitatively evaluate the anti-force performance and anti-moment performance separately, the following indices inspired by existing radius-based indices are introduced.

Force margin index (FMI): The radius of the inscribed sphere centered at the force state point in the force convex hull. It characterizes the ability of the CDPR to resist external force, output force, and generate acceleration in all directions at the current pose.

Moment margin index (MMI): The radius of the inscribed sphere centered at the moment state point in the moment convex hull. It characterizes the ability of the CDPR to resist external moment, output moment, and generate angular acceleration around all directions at the current pose.

It should be noted that the anti-force performance and anti-moment performance are not independent with each other. The change of wrench state will cause the change of force/moment convex hull accordingly due to the changes of the cross-section. When external force is applied on the end effector of CDPR, the anti-moment performance will change. And when an external moment is applied on the end effector of CDPR, the anti-force performance will also change. The decomposition process is not to completely decouple them, but to separately evaluate the ability to resist pure external forces or pure external moment. The significance of the proposed method lies in analyzing and optimizing the anti-disturbance performance based on its known parameters and loads. It transforms the problems of a 6-dimensional wrench space into problems of two 3-dimensional spaces, reducing the abstractness, avoiding the dimensional inconsistency, and having clear physical significance. Indices to quantify the relationship between the anti-force performance and the anti-moment performance will be analyzed in our subsequent research.

3.4 Improvement strategy with auxiliary branches

When the anti-disturbance performance of CDPR cannot meet the design requirements, the improvement strategy should be determined based on the position relationship between the force/moment state point and the corresponding convex hull.

There are mainly two cases. Case I is that the force/moment state point is close to the boundary of a convex hull, indicating that the potential of the actuation units has not been fully utilized. In this case, by installing auxiliary branches and applying proper auxiliary forces, the force/moment state point can be moved away from the boundary, thereby increasing the anti-disturbance performance. Case II is that the force/moment state point is near the central area of a small convex hull, indicating that the potential of anti-disturbance performance is insufficient. In this case, configuration and parameters should be adjusted to enlarge the corresponding convex hull.

In response to Case I, which is common in suspended CDPRs, we propose a strategy to improve the anti-disturbance performance based on auxiliary branches. For a CDPR with s auxiliary branches installed on the end effector, the unit direction vector of each auxiliary branch is $\boldsymbol{e}_{ai}$, the vector from the center of the end effector to the connecting point of each auxiliary branch is $\boldsymbol{c}_{ai}$, and the unit rotation vector is $\boldsymbol{u}_{ai}=\boldsymbol{c}_{ai}\times\boldsymbol{e}_{ai}$. When the auxiliary force provided by the i^{th} auxiliary branch is F_{ai}, the auxiliary force vector is $\boldsymbol{F}_{ai}=F_{ai}\boldsymbol{e}_{ai}$, and the auxiliary moment vector is $\boldsymbol{M}_{ai}=F_{ai}\boldsymbol{u}_{ai}$. Therefore, the comprehensive effect of the auxiliary branch is $\hat{\boldsymbol{Q}}_a=[\hat{\boldsymbol{F}}_a^T\ \ \hat{\boldsymbol{M}}_a^T]$.

$$\begin{aligned}&\hat{\boldsymbol{F}}_a^T=\sum_{i=1}^{s}F_{ai}\boldsymbol{e}_i=\boldsymbol{E}_a^T\boldsymbol{F}_a,\boldsymbol{E}_a=[\boldsymbol{e}_{a1}\quad\ldots\quad\boldsymbol{e}_{as}]^T,\boldsymbol{F}_a=[F_{a1}\quad\ldots\quad F_{as}]^T\\&\hat{\boldsymbol{M}}_a^T=\sum_{i=1}^{s}F_{ai}\boldsymbol{u}_i=\boldsymbol{U}_a^T\boldsymbol{F}_a,\boldsymbol{U}_a=[\boldsymbol{u}_{a1}\quad\ldots\quad\boldsymbol{u}_{as}]^T\end{aligned}\tag{11}$$

Define the origin wrench state point of the CDPR as $\hat{\boldsymbol{Q}}_{e0}=[\hat{\boldsymbol{F}}_{e0}^T\ \ \hat{\boldsymbol{M}}_{e0}^T]^T$. The new wrench state point under the actuation of auxiliary branches is $\hat{\boldsymbol{Q}}_e=\hat{\boldsymbol{Q}}_a+\hat{\boldsymbol{Q}}_{e0}$. And the new force state point in the force space can be defined as $\hat{\boldsymbol{F}}_e=\hat{\boldsymbol{F}}_a+\hat{\boldsymbol{F}}_{e0}$. Then, the distance from the new wrench state point to the hyperplanes that construct the force convex hull in the force space is:

$$\begin{aligned}&\boldsymbol{d}_F=(-\boldsymbol{W}^T\hat{\boldsymbol{Q}}_e+\boldsymbol{b})./\boldsymbol{w}_F=(-(\boldsymbol{W}_F^T\boldsymbol{E}_a^T+\boldsymbol{W}_M^T\boldsymbol{U}_a^T)\boldsymbol{F}_a-\boldsymbol{W}^T\hat{\boldsymbol{Q}}_{e0}+\boldsymbol{b})./\boldsymbol{w}_F\\&\boldsymbol{W}_F=[\boldsymbol{w}_{F1}\quad\boldsymbol{w}_{F2}\quad\boldsymbol{w}_{F3}],\boldsymbol{W}_M=[\boldsymbol{w}_{M1}\quad\boldsymbol{w}_{M2}\quad\boldsymbol{w}_{M3}],\boldsymbol{w}_F=[\|\boldsymbol{w}_{F1}\|\quad\|\boldsymbol{w}_{F2}\|\quad\|\boldsymbol{w}_{F3}\|]^T\end{aligned}\tag{12}$$

in which, $\boldsymbol{W}_F$ is the force sub-matrix of the normal matrix $\boldsymbol{W}$, which is a $k\times3$ matrix in 3-dimensional force space. k is the number of hyperplanes. $\boldsymbol{w}_{Fi}$ is the i^{th} column of $\boldsymbol{W}_F$. The $./$ operation represents dividing by elements. For any two k-dimensional vectors $\boldsymbol{a}=[a_1\quad\ldots\quad a_k]^T$ and $\boldsymbol{b}=[b_1\quad\ldots\quad b_k]^T$, the result of this operation is $\boldsymbol{a}./\boldsymbol{b}=[a_1/b_1\quad\ldots\quad a_k/b_k]^T$.

d_i is the i^{th} element of $\boldsymbol{d}_F=[d_1\quad\ldots\quad d_k]^T$. It represents the distance from the new force state point to the hyperplane corresponding to the i^{th} row of $\boldsymbol{W}_F$. If d_i is positive, the wrench state point is in the inside of the hyperplane, which is the side that leans towards the interior of the force convex hull. As mentioned in Section 3.2 and 3.3, the radius R_f of the maximum inscribed sphere of the force convex hull centered at $\hat{\boldsymbol{F}}_e$ represents the anti-force performance. Here, the values of R_f changes with the auxiliary force $\boldsymbol{F}_a$, and is expressed as $radius(\boldsymbol{F}_a)$, in which $radius(\boldsymbol{F}_a)=\min(\boldsymbol{d}_F)$.

If the force state point is farther away from the boundary of the force convex hull, larger FMI can be obtained. Thus, the objective is to maximize $radius(\boldsymbol{F}_a)$, and the problem is transformed into the following optimization problem:

$$\begin{aligned}&\text{Maximize:}\quad radius(\boldsymbol{F}_a=[F_{a1},\cdots,F_{ai}])\\&\text{Subject to:}\quad F_{ai\min}\le F_{ai}\le F_{ai\max},\ i=1,2,...,s\\&\qquad((\boldsymbol{w}_{Fj}^T\boldsymbol{E}_a^T+\boldsymbol{w}_{Mj}^T\boldsymbol{U}_a^T)\boldsymbol{F}_a+\boldsymbol{w}_j^T\hat{\boldsymbol{Q}}_{e0}-b_j)\le0,\ j=1,2,...,k\end{aligned}$$

At the given pose, $\boldsymbol{W}$, $\boldsymbol{b}$, $\boldsymbol{E}_a$, $\boldsymbol{U}_a$, $\hat{\boldsymbol{Q}}_{e0}$ are all known. The wrench set that the CDPR is able to output or resist is the AWS, which is a polyhedron in the wrench space. The wrench set that the auxiliary branches can provide also forms a polyhedron in the wrench space. We define it as Available Auxiliary wrench Set (AAS). The maximum dimension of the AAS is $\min(s,n)$, in which s is the number of auxiliary

branches, and n is the number of DOFs of the CDPR. The shape and position of the AAS are determined by the number and types of auxiliary branches, which can be line segments, polygons, polyhedrons, etc. The process of constructing AAS is similar to constructing AWS. The number and type of auxiliary branches determine the dimension of AAS. And the arrangement of auxiliary branches determines the shape of AAS. For example, assuming that the auxiliary branch used only drives one DOF, when one auxiliary branch is used, the AAS is a line segment. When two auxiliary branches are used and they are not collinear, the AAS is a polygon. When three auxiliary branches are used and they are not coplanar, the AAS is a polyhedron.

It should be noted that other types of auxiliary branches and devices are also suitable for the proposed method. And the shape of AAS can be various according to the type of device. For example, a tilting rotor [42] installed on the end effector can provide auxiliary force and moment. The magnitude of the auxiliary force and moment depends on the rotor speed, and the direction depends on the orientation of the tilting rotor. The shape of the AAS of the tilt-rotor can be regarded as a sector in the wrench space.

The process of determining the optimal auxiliary forces is equal to searching an optimal point in the AAS, which is farthest from the boundary of the force convex hull. The process to obtain the optimal auxiliary forces that maximize the MMI is similar, in which the objective becomes to $radiusM(\boldsymbol{F}_a) = \min(\boldsymbol{d}_M)$

$$\boldsymbol{d}_M = -(\boldsymbol{W}_F^T \boldsymbol{E}_a^T + \boldsymbol{W}_M^T \boldsymbol{U}_a^T)\boldsymbol{F}_a - \boldsymbol{W}^T \hat{\boldsymbol{Q}}_{e0} + \boldsymbol{b}). / \boldsymbol{w}_M \tag{13}$$

It should be noted that moment will be introduced when the auxiliary force is not applied at the center of the end effector, and the shapes of both force convex hull and moment convex hull will change. In some cases, applying auxiliary force may result in a larger FMI but a smaller MMI. To avoid this problem and improve the overall anti-moment performance, the MMI can be used as a constraint by adding a corresponding penalty function in programming. For example, adding a judgment statement to the objective function is a convenient approach, in which, when MMI is less than the desired target value, the outputted FMI is set to zero. By using this judgment statement, the results with insufficient MMI will be removed. In addition, by defining a Pareto front and conducting multi-objective optimization, more comprehensive anti-disturbance performance can be achieved, which will be an important part of our further research.

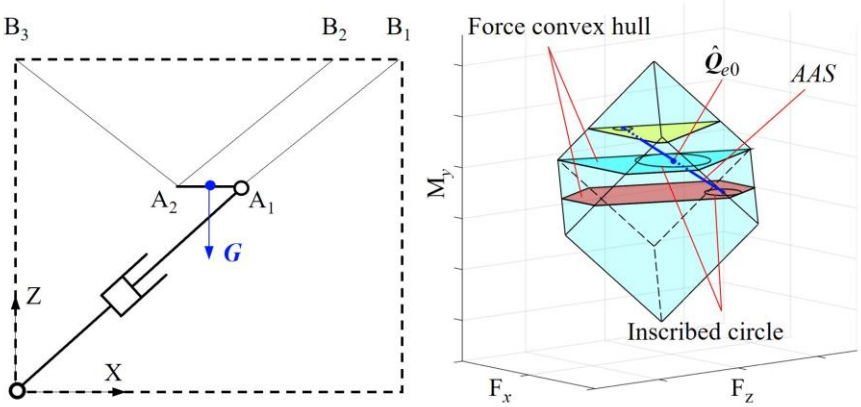

(a). Kinematic model (b). Force convex hulls with different auxiliary forces

Figure 8: An example of the improvement strategy

Take the planar 3-cable CSPR as an example. Assuming a rigid RPR branch is connected at A_1 on the end effector as the auxiliary branch, as shown in Fig. 8(a), the auxiliary branch is only used to provide auxiliary force and does not participate in position control. As shown in Fig. 8(b), at a given pose, the AAS is a line segment in the 3-dimensional wrench space. Each point on the line segment represents a possible wrench state point with the help of auxiliary force. Take a cross-section parallel to the plane $\{O - F_x F_z\}$ at a certain point on the line segment. The cross-section is the force convex hull at this point. Geometrically, determining auxiliary force is equal to finding a special point on the line segment. The inscribed circle of the cross-section centered at this point in AAS has larger radius than that of other points.

4. Analysis of anti-disturbance performance

4.1 Anti-disturbance performance of the CDFP

The FMI and MMI are adopted to analyze the anti-disturbance performance of the CDFP. The performance is plotted in polar coordinate, as shown in Fig. 9. The polar axis corresponds to the zenith angle, and the polar angle corresponds to the direction angle. In which, the range of zenith angle is [0, 50°], and the range of direction angle is [0, 360°).

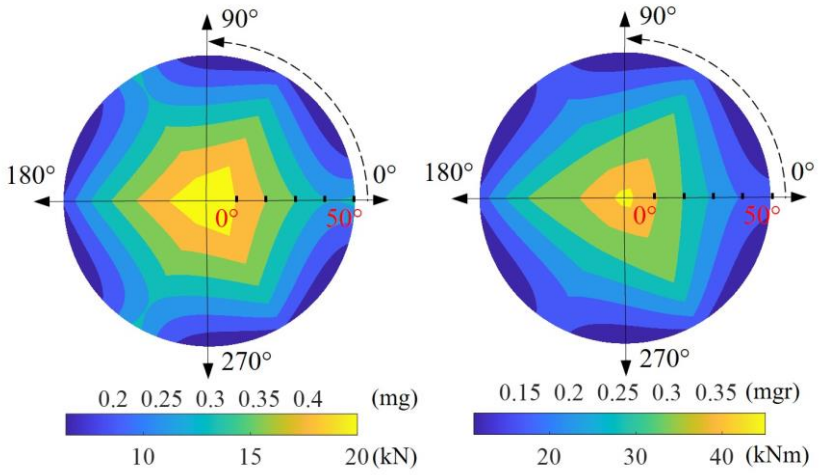

(a) FMI (b) MMI

Figure 9: The anti-force performance and anti-moment performance of the CDFP

The anti-disturbance performance of suspended CDPR is greatly affected by the force due to gravity, which is mainly decided by the mass of the end effector (including the load). Therefore, we divide the FMI by the force due to the gravity of the end effector, and the unit of FMI is normalized from "N" to "mg", which represents how many times the FMI is the gravity of the end effector. Similarly, we divide the MMI by the force due to the gravity of the end effector and multiply it by the radius of the distribution circle of anchor points, which is referred to in the Appendix. Then, the unit of MMI is normalized from "Nm" to "mgr".

The maximum cable tension of the CDFP is selected as 1mg (42.14kN). The minimum cable tension is selected as 1kN to prevent the cable from leaving the pulleys due to too little tension [43], which is 1% of the breaking load of the selected 14mm steel cable (104kN).

The FMI and MMI of CDFP are much larger when the zenith angle is small, compared with the FMI and MMI when the zenith angle is large. The maximum FMI is 0.49mg(20.78kN), and the maximum MMI is 0.42mgr(45.81kNm). This indicates that the CDFP is able to resist external force up to 0.49mg(20.78kN) or external moment up to 0.42mgr(45.81kNm) in any direction, and cables will not be slack or overloaded.

The FMI and MMI decrease rapidly with the increase of the zenith angle. And due to the centrosymmetric configuration of CDFP, the performance distribution is centrosymmetric. The FMI and MMI are larger when the direction angle is at 0°, 60°, and 120° compared with FMI and MMI in other direction angles, which are integer multiples of 60°. At the maximum zenith angle (50°), the average value of the FMI is 0.19mg(8.01kN), and the minimum value is 0.15mg(6.32kN). The average value of the MMI is 0.13mgr(14.25kNm), and the minimum value is 0.10mgr(10.95kNm). The anti-force performance and anti-moment performance are only 30% to 40% of that of the central region.

In addition, at the maximum zenith angle (50°), the standard deviation of FMI and MMI are 0.045mg(1.90kN) and 0.022mgr(2.43kNm), which are 24% and 17% of the mean value of FMI and MMI. This indicates that the FMI and MMI at the maximum zenith angle are not only small but also unevenly distributed.

To visually observe the anti-disturbance performance at large zenith angles, the force and moment convex hulls with zenith angle of 50° and direction angle of 30° are plotted in Fig. 10. The red dots represent the force/moment state points. The blue dots represent the tangent points of the inscribed sphere of force/moment convex hulls centered at red dots. The lines connecting the red dots to the blue dots are the weakest direction to resist external force/moment. The two orange spheres represent the

inscribed spheres centered at the force/moment state points.

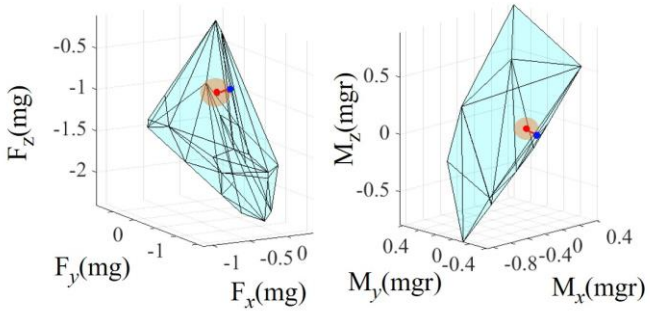

(a) Force convex hull (b) Moment convex hull

Figure 10: Force and moment convex hulls with zenith angle of 50°

The volumes of the force and moment convex hulls are much larger than the inscribed spheres, showing that CDFP has good potential to resist and output force and moment. The reason for the current low margin is that the force/moment state points are close to the boundary of the force/moment convex hulls. And the weak directions severely limit the performance. By installing auxiliary branches and exerting proper force on the end effector, the potential of the CDFP can be unleashed, and the anti-disturbance performance can be improved.

The operational status of FAST under different wind conditions is governed by the operational guidelines established by the CAS Key Laboratory of FAST, which are formulated based on the design documents and historical wind force data for FAST [4]. According to the historical data, on the majority of days at the FAST location, wind forces do not exceed Beaufort four-level, with the extreme maximum wind force reaching Beaufort nine-level. Consequently, FAST is designed to operate effectively under a maximum wind force of Beaufort four-level. As an additional safety precaution, the CAS Key Laboratory of FAST stipulates that the feed cabin must be moved to the ground when the wind reaches Beaufort eight-level.

The shape of the end effector is symmetrical, and the gravity center is located at the geometric center through balancing. The maximum wind speed under Beaufort eight-level is 20.7m/s, and the effective wind area of the end effector of CDFP is about $30m^2$. According to the wind force formula, the maximum wind force on the end effector of CDFP under Beaufort eight-level wind is 7.87kN, which is about 0.18mg. In order to maintain sufficient margin to ensure that the CDFP does not lose control, the FMI is selected to be greater than 0.3mg with a safety factor of 1.6. And the MMI is selected to be greater than 0.1mgr.

Considering the constraints of installation space and astronomical observation tasks, UPS branches are adopted to improve the anti-disturbance performance of the CDFP. One and three branches are separately equipped and analyzed in the following Sections. The six cables of the CDFP adopt position control, and the auxiliary branches adopt force control.

4.2 CDFP equipped with one UPS auxiliary branch

The CDFP with one UPS auxiliary branch is shown in Fig. 11. An UPS branch is installed between the base and end effector. The upper end of the branch is connected with the base through a universal joint. And the lower end is connected with the end effector through a spherical joint composed of a universal joint and a rotating joint.

For the CDFP, if the force of auxiliary branch is applied to the center of the end effector, the anti-disturbance performance can be improved. Since the upper surface of the receivers is 1.6m above the end effector, the lower joint of the auxiliary branch is installed 1.9m above the center of the end effector to avoid interference. In addition, the upper joint of the auxiliary branch is 1.15m above the center of the base because the frame that provides the installation location is 1.45m above the base. Therefore, extra moment will be introduced when applying auxiliary force.

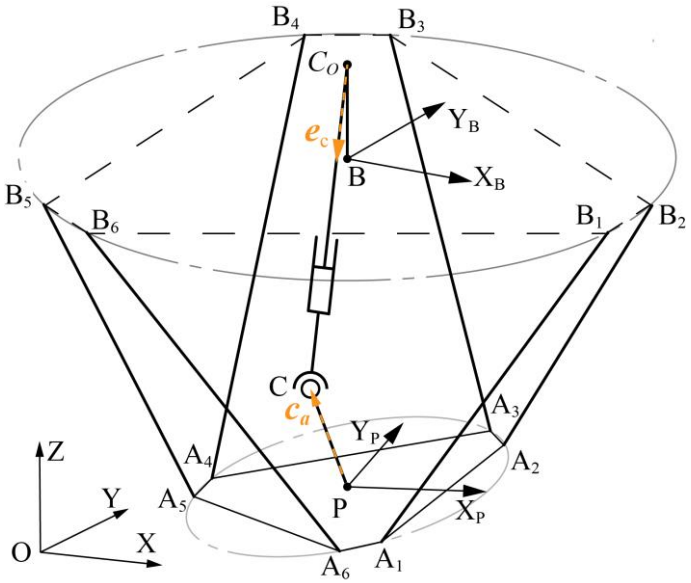

Figure 11: Kinematic model of CDFP with one UPS auxiliary branch

As is shown in Fig. 11, the upper joint of the UPS branch is C_O, and the lower joint is C. C_O is 1.15m above the geometric center of the base. C is 1.9m above the geometric center of the end effector. The vector from the geometric center P to the lower joint C is $\boldsymbol{c}_a$. The vector of the UPS branch from C_O to C is $\boldsymbol{c}$, the unit direction vector is $\boldsymbol{e}_c$, and the unit rotational vector is $\boldsymbol{u}_a = \boldsymbol{c}_a \times \boldsymbol{e}_c$. Assuming that the force provided by the auxiliary branch is F_c, when the force due to gravity is considered, the FMI is:

$$radius(F_c) = \min(-F_c(\boldsymbol{W}_F^T \boldsymbol{e}_c + \boldsymbol{W}_M^T(\boldsymbol{c}_a \times \boldsymbol{e}_c)) - \boldsymbol{W}^T \hat{\boldsymbol{Q}}_{e0} + \boldsymbol{b}). / \boldsymbol{w}_F \tag{14}$$

And the MMI is:

$$radiusM(F_c) = \min(-F_c(\boldsymbol{W}_F^T \boldsymbol{e}_c + \boldsymbol{W}_M^T(\boldsymbol{c}_a \times \boldsymbol{e}_c)) - \boldsymbol{W}^T \hat{\boldsymbol{Q}}_{e0} + \boldsymbol{b}). / \boldsymbol{w}_M \tag{15}$$

Considering that the MMI has met the design requirements, the FMI is selected as the objective to determine the auxiliary force. The MMI is regarded as a constraint, and is implanted as a penalty function in the optimization, in which, when MMI is smaller than 0.1mgr, the outputted FMI is set as zero. The process of determining the optimal force of the auxiliary branch is actually to find an optimal point. And the optimization problem can be transformed into:

$$\begin{aligned} &\text{Maximize:} \quad radius(F_c) \\ &\text{Subject to:} \quad F_{c\min} \le F_c \le F_{c\max} \\ &\qquad (F_c(\boldsymbol{w}_{Fi}^T \boldsymbol{e}_c + \boldsymbol{w}_M^T \boldsymbol{u}_c) + \boldsymbol{w}_i \hat{\boldsymbol{Q}}_{e0} - b_i) \le 0, i = 1,2,...,6 \\ &\qquad radiusM(F_c) \ge 0.1mgr \end{aligned}$$

The maximum and minimum auxiliary force is ± 0.3mg, in which positive value represents downward force and negative value represents upward force. The FMI/MMI and auxiliary force of the CDFP at different direction angles and zenith angles are shown in Fig. 12(a)~(c). It can be seen that the FMI and MMI of the CDFP have been significantly improved with the auxiliary branch. At the maximum zenith angle of 50°, the average FMI is increased to 0.40mg(16.86kN), and the minimum value is 0.36mg(15.17kN). The average MMI is 0.25mgr(27.39kNm), and the minimum value is 0.21mgr(23.01kNm). Compared to the CDFP without the auxiliary branch, the average FMI increases by 110%, and the minimum value increases by 140%. The average MMI increases by 92%, and the minimum value increases by 110%. The increase in MMI is because that auxiliary force also moves the moment state point further away from the boundary of moment convex hull.

At the maximum zenith angle (50°), the standard deviation of FMI and MMI are 0.025mg(1.06kN) and 0.042mg(4.58kNm), which are 6.25% and 17% of the mean value of FMI and MMI. The uniformity of the FMI at the maximum zenith angle has been improved. The standard deviation value of MMI has increased a bit, but the ratio of it to the mean value of MMI has changed very little.

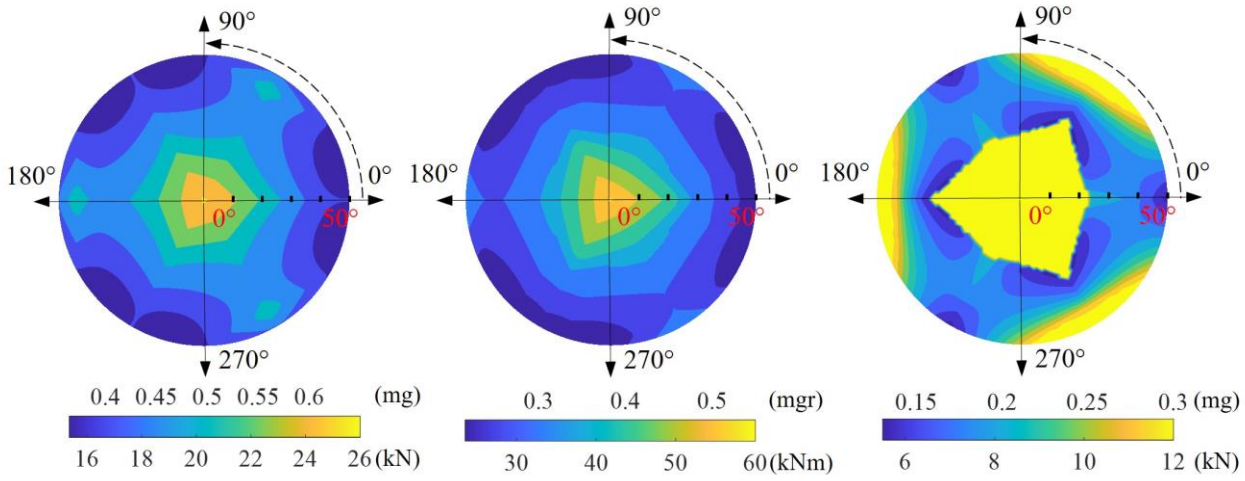

(a) FMI (b) MMI (c) Auxiliary force

Figure 12: FMI, MMI, and the auxiliary force of CDFP with one auxiliary branch

As shown in Fig. 12(c), the auxiliary force is not as large as possible. When the zenith angle is small, the additional moment is small, and a large downward auxiliary force is beneficial, as shown in the yellow central area. When the zenith angle approaches 50°, the auxiliary force needs to be chosen rationally, as shown in the boundary area. There is a mutation in the optimal auxiliary force between the two regions. Since CDFP already has good anti-disturbance performance when the zenith angle is small, the auxiliary force can start working only at large zenith angles to avoid the impact of drastic changes in auxiliary force.

4.3 CDFP equipped with three UPS auxiliary branches

The CDFP with three UPS auxiliary branches is also designed. As shown in Fig. 13, the upper joint of the i^{th} UPS branch is C_{Oi}, and the lower joint is C_i. $C_{O1} \sim C_{O3}$ are central symmetrically distributed on the plane 1.15m above the base, and connected with the base. The radius r_a of the distribution circle is 3m. $C_1 \sim C_3$ are centrally symmetrically distributed on the plane 1.9m above the end effector, and connected with the end effector. The radius r_c of the distribution circle is 0.1m. The vector from the geometric center of the end effector P to the i^{th} lower joint C_i is $\boldsymbol{c}_{ai}$. The vector of the i^{th} UPS branch from C_{oi} to C_i is $\boldsymbol{c}_i$, its unit direction vector is $\boldsymbol{e}_{ci}$, and the unit rotational vector is $\boldsymbol{u}_i = \boldsymbol{c}_{ai} \times \boldsymbol{e}_{ci}$. Define the matrix $\boldsymbol{E}_c$ and $\boldsymbol{U}_a$ to present the unit direction vectors and unit rotational vectors:

$$\boldsymbol{E}_c = [\boldsymbol{e}_{c1} \quad \boldsymbol{e}_{c2} \quad \boldsymbol{e}_{c3}]$$
$$\boldsymbol{U}_a = [\boldsymbol{u}_1 \quad \boldsymbol{u}_2 \quad \boldsymbol{u}_3]$$

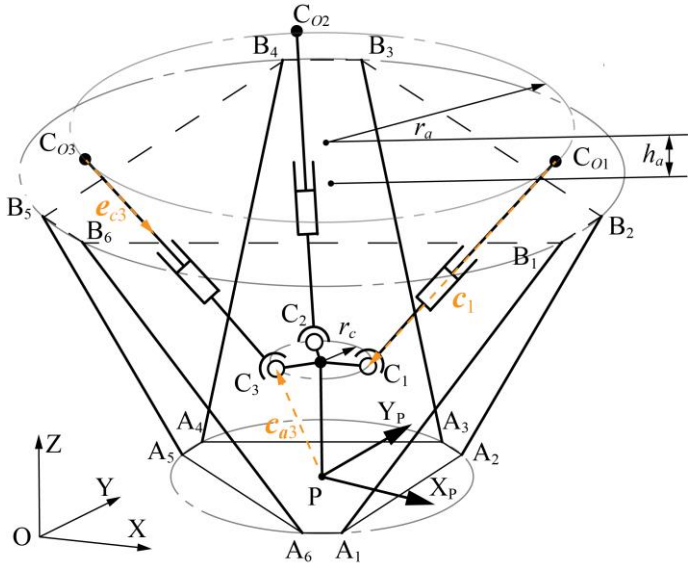

Figure 13: Kinematic model of the CDFP with three UPS auxiliary branches

Assuming that the force provided by the auxiliary branches are $\boldsymbol{F}_c = [F_{c1} \quad F_{c2} \quad F_{c3}]^T$, when the force due to gravity is exerted to the end effector, the FMI is:

$$radius(\boldsymbol{F}_c) = \min(-(\boldsymbol{W}_F^T \boldsymbol{E}_c^T + \boldsymbol{W}_M^T \boldsymbol{U}_c^T)\boldsymbol{F}_c - \boldsymbol{W}^T \hat{\boldsymbol{Q}}_{e0} + \boldsymbol{b}) ./ \boldsymbol{w}_F \tag{16}$$

And the MMI is:

$$radiusM(\boldsymbol{F}_c) = \min(-(\boldsymbol{W}_F^T \boldsymbol{E}_c^T + \boldsymbol{W}_M^T \boldsymbol{U}_c^T)\boldsymbol{F}_c - \boldsymbol{W}^T \hat{\boldsymbol{Q}}_{e0} + \boldsymbol{b}) ./ \boldsymbol{w}_M \tag{17}$$

At the given pose, the AAS that can be provided by the auxiliary branches forms a parallelepiped in the wrench space. The process of solving the optimal auxiliary force is to find an optimal point in the parallelepiped. And the optimization problem can be transformed into:

$$\begin{aligned}
&\text{Maximize:} \quad radius(\boldsymbol{F}_c) \\
&\text{Subject to:} \quad F_{c\min} \le F_{ci} \le F_{c\max}, i = 1,2,3 \\
&\qquad ((\boldsymbol{w}_{Fi}^T \boldsymbol{E}_c^T + \boldsymbol{w}_M^T \boldsymbol{U}_c^T)\boldsymbol{F}_c + \boldsymbol{w}_i \hat{\boldsymbol{Q}}_{e0} - b_i) \le 0, i = 1,2,...,6 \\
&\qquad radiusM(\boldsymbol{F}_c) \ge 0.1mgr
\end{aligned}$$

The maximum and minimum auxiliary forces are also ± 0.3mg. The auxiliary force and FMI/MMI of the CDFP are shown in Fig. 14. Considering the rotational symmetry of the three auxiliary branches, the force of the first auxiliary branch is given.

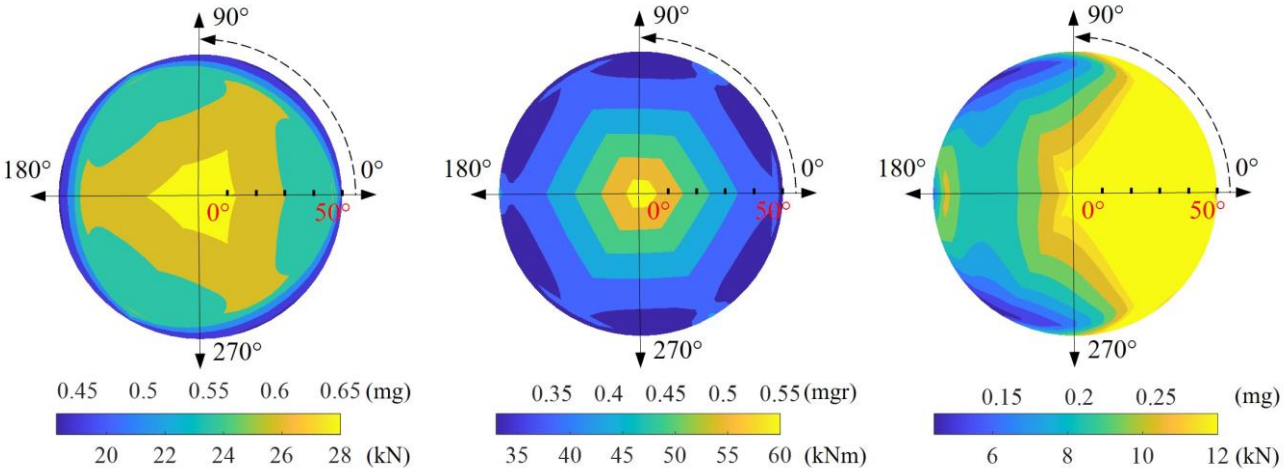

(a) FMI (b) MMI (c) Force of first auxiliary branch

Figure 14: FMI, MMI, and the auxiliary force of CDFP with three auxiliary branches

With the auxiliary branches, the FMI and MMI are further enhanced. At the maximum zenith angle of 50°, the average FMI is increased to 0.45mg(18.96kN), and the minimum value is 0.43mg(18.12kN). The average MMI at the maximum zenith angle is 0.32mgr(35.06kNm), and the minimum value is 0.30mgr(32.87kNm). Compared to the scheme without auxiliary branch, the average FMI increases by 137% and the minimum value increases by 186%. The average MMI increases by 146%, and the minimum value increases by 200%.

At the maximum zenith angle (50°), the standard deviation of FMI and MMI are 0.012mg(0.52kN) and 0.029mgr(3.17kNm), which are 3% and 9% of the mean value of FMI and MMI. The uniformity of FMI and MMI has been improved.

The anti-disturbance performance of the CDFP with three auxiliary branches is further improved compared to the scheme with one branch. This is because the AAS provided by the three UPS branches forms a 3-dimensional parallelepiped, which provides more choices for the wrench stated point. And the wrench state point can be moved further away from the boundary of AWS.

The auxiliary forces need to be solved through the iterative optimization. In this research, a computer with the CPU of Intel Core i7-12700F(2.10GHz) and a RAM of 16GB is adopted, and the fmincon function in the MATLAB software is used for the convenience of programming. Method II takes 14ms on average to solve the auxiliary force for the CDFP with one branch, and takes 32ms on average for the CDFP with three branches, which meets the requirement for online solving and control of the FAST with the control period of 200ms. The time cost of method I are 0.97s and 10.6s, which is slower. Method I has lower efficiency, it can be used to visually analyze directional anti-disturbance

performance and auxiliary branch design because force/moment convex hull can be plotted based on the solving results.

5. Simulation and verification

Simulations under typical working states are conducted to show the tension distribution of the CDFP. The maximum angular velocity and angular acceleration of the CDFP are only 1.2×10^{-3} rad/s (0.0688°/s) and 6.0×10^{-5} rad/s^2. The forces caused by the terms of velocity and acceleration in dynamic models are less than 1% of the force due to gravity. Therefore, a quasi-static approach is adopted in the simulation.

During the simulation, the auxiliary branches apply pre-calculated auxiliary forces to the end effector. Good force servo accuracy can be achieved because CDFP runs slowly and stably, resulting in slow changes in auxiliary forces. According to the supplier of the auxiliary branch, the force servo accuracy is about ±10% of the maximum auxiliary force. Therefore, Gaussian white noise with a range of [-1.20kN, 1.20kN] is introduced to the force of each auxiliary branch.

The rotation from the horizontal state to the maximum zenith angle at the maximum angular velocity is simulated to show the distribution of cable tensions. The direction angle is 30°, which is the weakest direction according to the analysis, and the zenith angle increases from 0° to 50° at an angular velocity of 0.05°/s.

As shown in Fig. 15(a)~(c), when the zenith angle is large, the cable tension difference of the CDFP without auxiliary branch is large, and the minimum cable tension is only 4.10kN. By installing one or three auxiliary branches and applying auxiliary forces, the minimum cable tension increases to 8.62kN and 10.41kN, reducing the risk of cable slack. There is a sudden change of tensions for CDFP with one auxiliary branch at 224s. The sudden change of tensions is due to the sudden change of auxiliary force, which can be seen in the central area of Fig. 12(c). In practice, auxiliary force at the sudden change position can be smoothed by using a smooth curve, which eliminates the sudden change of auxiliary force and tensions. The force servo error of the auxiliary branches will cause fluctuation of tensions, but the fluctuation is relatively small compared to the overall cable tension. It indicates that the auxiliary branch can effectively increase the minimum cable tension, keep the cables away from slack, and enhance the anti-disturbance performance of the CDFP.

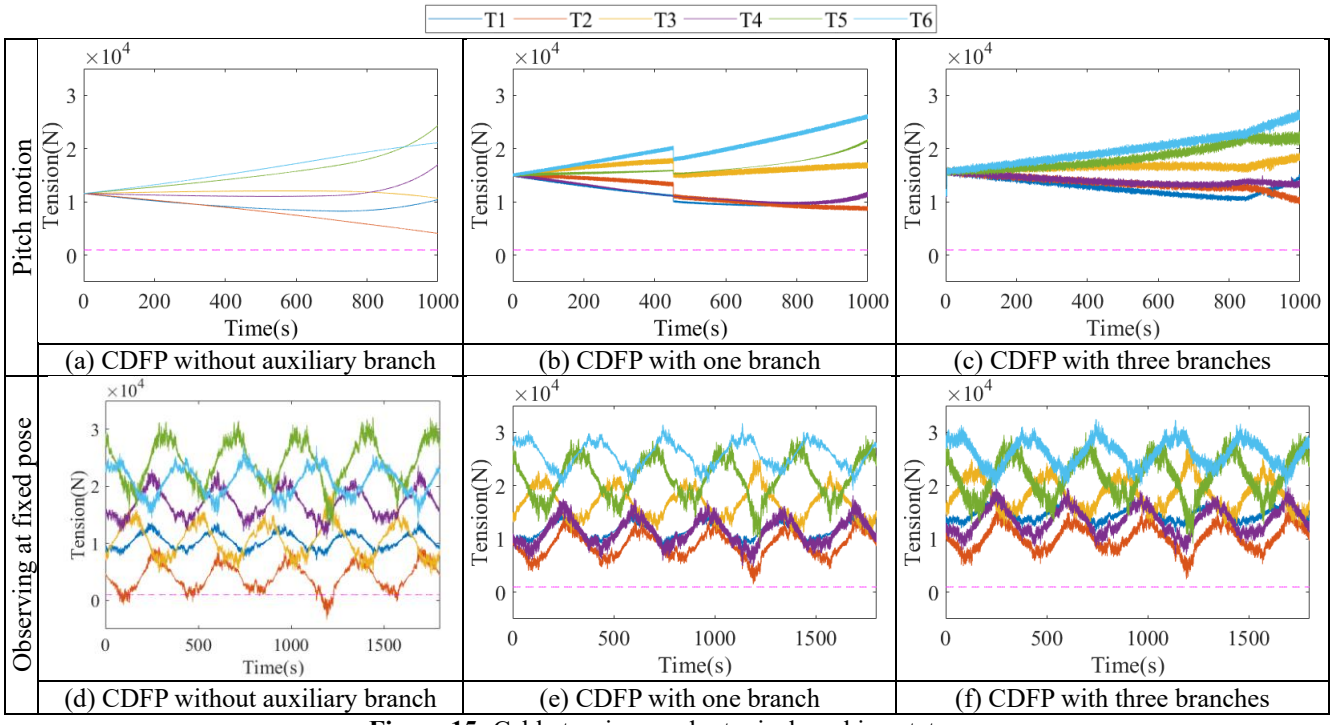

Figure 15: Cable tensions under typical working states

Furthermore, the anti-disturbance performance and cable tensions at the extreme observation pose are simulated. Assuming the CDFP keeps stationary at the extreme observation pose to receive signals with the direction angle of 30° and the zenith angle of 50°, and the wind force reaches Beaufort eight-level,

which is the maximum wind force that needs to be resisted. Therefore, external wind disturbance with an average wind speed of 20.7m/s is applied, which is the maximum wind speed under Beaufort eight-level. The Davenport wind spectrum is used to simulate fluctuating components. In which, the gust velocity is obtained by inputting a white-noise signal of unit standard deviation into the approximation filter of the Davenport spectrum [2]. The effective wind area of the end effector is 30m^2 to simulate the situation where the windward surface of the end effector is the largest surface. Assume that the wind direction is mainly horizontal and changes during the process to simulate disturbances in various directions. The wind force on the end effector is as shown in Fig. 16, in which the wind direction changes at a speed of 1°/s from 0° to 360° for five cycles.

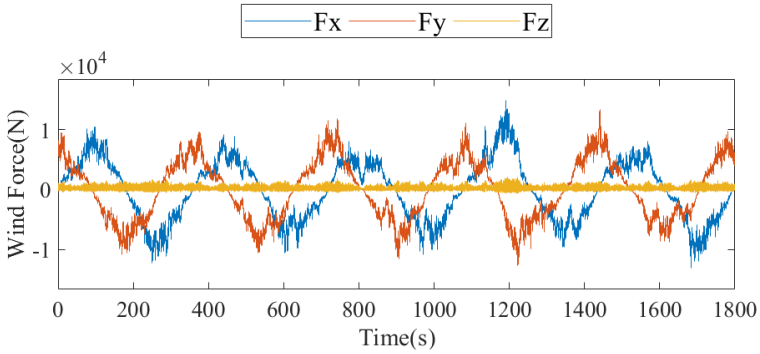

Figure 16: Wind disturbance force on the end effector

The simulation results of tension distribution for the three schemes subjected to external wind disturbances are shown in Fig. 15(d)~(f). It can be seen that under wind forces, the minimum tension of the CDFP without the auxiliary branch is small. In some cases, the tension is smaller than the minimum tension constraint (1kN), which is represented as the dashed line. As for the CDFP with one branch, the minimum cable tension has been increased to 1.42kN. And the minimum cable tension of CDFP with three auxiliary branches is 3.37kN. The percentage of cases where some cable tensions are lower than the minimum tension constraint (1kN) is 6.9%, 0%, and 0% for CDFP with zero, one, or three auxiliary branches, indicating the effect of the auxiliary branches to improve the anti-disturbance performance.

The maximum cable tension of CDFP with zero, one, and three auxiliary branches are all around 31kN. The average values of the average tension of the six cables in 0~1800s for CDFPs with one or three auxiliary branches increase by 9.8% and 20.4% compared with CDFP without auxiliary branches.

By installing one or three branches, the anti-disturbance performance is effectively improved, and the risk of slack is reduced. The maximum cable tension of the three CDFPs are almost equal. When selecting motors, the maximum torque of the selected motors for the three schemes can be the same. And CDFPs with auxiliary branches need motors with larger rated torque due to the larger average tension. The minimum tension and average tension of the CDFP with three auxiliary branches are the largest. The CDFP with one auxiliary branch has a simpler and lighter structure compared to the three-branch scheme. Finally, the CDFP with one branch is selected as the final upgrade design scheme for the FAST to carry out detailed engineering design and experimental research.

The CDFP significantly reduces the self-weight, and the estimated mass of the cable-driven devices and the auxiliary branch is about 3000kg. The mass of the existing rigid fine-tuning platform including the A-B rotator and the Gough-Stewart parallel mechanism is about 7110kg.

6. Conclusion and future work

This paper proposes a novel method to visually analyze the anti-disturbance performance based on the AWS and the decomposition of convex polyhedrons in the wrench space. This method shows the anti-force performance and anti-moment performance intuitively and separately, avoiding dimensional inconsistency. The decomposition approaches of the AWS are established with the convex hull method and the hyperplane shifting method to meet the requirements of intuitiveness and solving efficiency. FMI/MMI indices are introduced to evaluate the anti-disturbance performance quantitatively. The proposed methods and indices have advantages of clear physical meaning, consistent dimensionality, high solving efficiency and good intuitiveness. The strategy to improve the anti-disturbance performance with the auxiliary branch is presented. The method of this paper can be used to analyze

and optimize the wrench output performance, resist external disturbance, and generate acceleration for CDPRs with translational, rotational, or hybrid DOFs.

A novel CDFP of the FAST is designed considering the anti-disturbance performance, which has the advantages of lightweight, heavy load and large rotation. Analysis and optimization of the disturbance resistance of the CDFP are implemented with the proposed methods. Auxiliary branches are adopted to improve the anti-disturbance performance. Two configurations of auxiliary branches are designed, which improve the anti-force performance of the CDFP under extreme observation poses by 140% and 186%. The driving units of the CDFP reduce weight by about 57%, and the observation zenith angle of FAST is increased by 25% to 50°. The CDFP with one auxiliary branch has been selected as the final design scheme. In the future, the 1:1 experimental prototype will be established to carry out further experiments. And we will also try to expand the proposed method in the analysis of more complex CDPRs like tendon-driven robot arms.

Acknowledgment

This work was supported by the National Natural Science Foundation of China (grant number U19A20101, 52105025) and the National High-tech Ship Research Project of China (grant number MC-202003-Z01). The authors would like to thank the editor and reviewers for their pertinent comments and suggestions.

Appendix. Modeling and Parameters of the CDFP

The kinematic model of the CDFP is illustrated in Fig. A1. B_1~B_6 are the cable outlet points on the base. A_1~A_6 are the cable anchor points on the end effector. r_1 is the radius of the distribution circle of cable outlet points. r_2 is the radius of the distribution circle of cable anchor points. φ_1 is the angle between two adjacent cable outlet points, while φ_2 is the angle between adjacent cable anchor points.

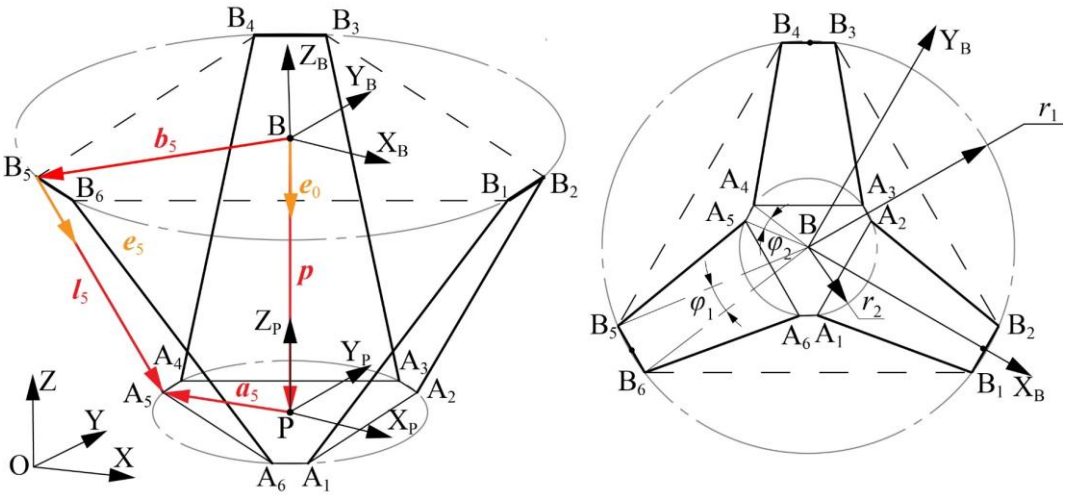

Figure A1: Kinematic model of the CDFP

$\{O-XYZ\}$ is the global coordinate system. Its unit direction vectors are $\boldsymbol{e}_x$ $\boldsymbol{e}_y$ $\boldsymbol{e}_z$. $\{B-X_BY_BZ_B\}$ is the base coordinate system, and the origin B is located at the center of the base. Its unit direction vectors are $\boldsymbol{e}_{Bx}$ $\boldsymbol{e}_{By}$ $\boldsymbol{e}_{Bz}$. $\{P-X_PY_PZ_P\}$ is the end coordinate system with the origin P located at the center of the end effector. Its unit direction vectors are $\boldsymbol{e}_{Px}$ $\boldsymbol{e}_{Py}$ $\boldsymbol{e}_{Pz}$.

The position vector from B to P is $\boldsymbol{p}$, and its unit vector is $\boldsymbol{e}_0$. $\boldsymbol{b}_i$ is the vector from B to the cable outlet point B_i. $\boldsymbol{a}_i$ is the vector from P to the cable anchor point A_i. The vector from cable anchor point A_i to cable outlet point B_i is $\boldsymbol{l}_i$, and its unit vector is $\boldsymbol{e}_i$.

${}^{O}_{B}\boldsymbol{R}$ is the rotation matrix from the base coordinate system to the global coordinate system. ${}^{B}_{P}\boldsymbol{R}$ is the rotation matrix from the end coordinate system to the base coordinate system. ${}^{O}_{P}\boldsymbol{R}$ is the rotation matrix from the end coordinate system to the global coordinate system.

The i^{th} cable vector is:

$$\boldsymbol{l}_i = -\boldsymbol{b}_i + \boldsymbol{a}_i + \boldsymbol{p} = -{}^{O}_{B}\boldsymbol{R}\,{}^{B}\boldsymbol{b}_i + {}^{O}_{P}\boldsymbol{R}\,{}^{P}\boldsymbol{a}_i + {}^{O}_{B}\boldsymbol{R}\,{}^{B}\boldsymbol{p} \tag{A1}$$

The unit direction vector of the i^{th} cable is:

$$\boldsymbol{e}_i = \boldsymbol{l}_i / |\boldsymbol{l}_i| \tag{A2}$$

The velocity and acceleration of the feed support system are low. The maximum angular velocity and angular acceleration of the CDFP are only 1.2×10^{-3} rad/s and 6.0×10^{-5} rad/s^2. The inertial force during motion is less than 1% of the force due to gravity. Therefore, statics model is adopted for analysis and simulation.

The Jacobian matrix of the CDPR is:

$$\boldsymbol{J} = \begin{bmatrix} \boldsymbol{e}_1 & \cdots & \boldsymbol{e}_6 \\ ({}^{O}_{P}\boldsymbol{R}\,{}^{P}\boldsymbol{a}_1)\times\boldsymbol{e}_1 & \cdots & ({}^{O}_{P}\boldsymbol{R}\,{}^{P}\boldsymbol{a}_6)\times\boldsymbol{e}_6 \end{bmatrix}^T = \begin{bmatrix} \boldsymbol{e}_1 & \cdots & \boldsymbol{e}_6 \\ \boldsymbol{u}_1 & \cdots & \boldsymbol{u}_6 \end{bmatrix}^T \tag{A3}$$

in which, $\boldsymbol{u}_i$ is called the unit rotation vector, and $\boldsymbol{u}_i = ({}^{O}_{P}\boldsymbol{R}\,{}^{P}\boldsymbol{a}_i)\times\boldsymbol{e}_i$.

The statics equation is:

$$-\boldsymbol{J}^T\boldsymbol{T} + \boldsymbol{q}_e = 0 \tag{A4}$$

in which $\boldsymbol{T} = [t_1 \ \cdots \ t_6]^T$ is the cable tension column array, and t_i is the tension on the i^{th} cable. $\boldsymbol{q}_e = [\boldsymbol{f}_e^T \ \ \boldsymbol{\tau}_e^T]^T$ is a column array that represents the external force and external moment acting on the end effector.

The optimization design is carried out to satisfy all constraints. The main constraints are as follows:

(1). The radius of the distribution circle of cable outlet points at the base should be smaller than 3.3m.

(2). The radius of the distribution circle of cable anchor points at the end effector should be smaller than 2.6m.

(3). The distance between the base and end effector should be close to 2m.

(4). Cables must not interfere with the end effector or receivers.

(5). Distance between the adjacent cable outlet points and adjacent cable anchor points should be larger than 0.3m.

The parameters are determined as shown in Table. A1.

Table A1: The main parameters of the CDPR

Parameter	Symbol	Value
The radius of the distribution circle of cable outlet points	r_1	3.3m
The radius of the distribution circle of cable anchor points	r_2	2.6m
The angle between each group of cable outlet point	φ_1	6°
The angle between each group of cable anchor point	φ_2	12°
The initial distance between the base and the end effector	p_z	2m
The total mass of the end effector	m	4300kg

According to the simulation, the optimized CDFP can achieve 100mm error compensation motion in any direction at any observation pose. When the end effector moves 100mm in any direction at any pose, the FMI maintains larger than 0.3mg, and the MMI maintains larger than 0.1mg.

The safety distance is the minimum distance between the cables and the surface of the receivers. According to the simulation, when the end effector moves 100mm in any direction at any pose, the safety distance is larger than 20mm.

The mass of the existing rigid fine-tuning platform is 3000kg. When the weight of the end effector increases, a Gough-Stewart parallel mechanism and A-B rotator with a larger load capacity are needed, which further increases the weight of the feed cabin. The load capacity of the first-level cable platform is approaching its limit. Therefore, it is difficult to add heavier receivers to the existing rigid fine-tuning platform.

By replacing the rigid fine-tuning platform with CDFP, the weight of the feed cabin can be reduced, making it possible to carry heavier feed sources. The total mass of the new end effector and receivers is 4300kg, which increases by 43% in weight.

References

[1] Qian L, Yao R, Sun J H, Xu J L, Pan Z C, Jiang P. FAST: Its scientific achievements and prospects. Innovation, 2020, 1(3).

[2] Shao Z F, Tang X Q, Wang L P, Chen X. Dynamic modeling and wind vibration control of the feed support system in FAST. Nonlinear Dynamics, 2012, 67(2):965-985.

[3] Tang X Q, Zhu W B, Sun C H, Yao R. Similarity model of feed support system for FAST. Experimental Astronomy, 2011, 29(3):177-187.

[4] Zhang Z K, Shao Z F, You Z, Tang X Q, Zi B, Yang G L, Gosselin C, Caro S. State-of-the-art on theories and applications of cable-driven parallel robots. Frontiers of Mechanical Engineering, 2022, 17(3).

[5] Han G, Li J, Chen Y, Wang S, Chen H. Dynamic modeling and motion control strategy of cable-driven cleaning robot for ship cargo hold. Journal of Marine Science and Engineering, 2023, 11(1):87.

[6] Chae H, Moon Y, Lee K, Park S, Kim H S, Seo T. A tethered façade cleaning robot based on a dual rope windlass climbing mechanism: design and experiments. IEEE/ASME Transactions on Mechatronics, 2022, 27(4):1982-1989.

[7] Zhang F, Shang W W, Zhang B, Cong S. Design optimization of redundantly actuated cable-driven parallel robots for automated warehouse system. IEEE Access, 2020, 8:56867-56879.

[8] Bruckmann T, Sturm C, Fehlberg L, Reichert C, IEEE. An energy-efficient wire-based storage and retrieval system. 3rd International Conference on Cable-Driven Parallel Robots (CableCon 2017), Quebec, QC, Canada, Aug. 2-4, 2013

[9] Wu Y L, Cheng H H, Fingrut A, Crolla K, Yam Y, Lau D. CU-Brick cable-driven robot for automated construction of complex brick structures: from simulation to hardware realisation. 2018 IEEE International Conference on Simulation, Modeling, and Programming for Autonomous Robots (SIMPAR 2018), Brisbane, Austrlia, May 16-19, 2018

[10] Bruckmann T, Reichert C, Meik M, Lemmen P, Spengler A, Mattern H, Konig M. Concept studies of automated construction using cable-driven parallel robots. 3rd International Conference on Cable-Driven Parallel Robots (CableCon), Quebec, QC, Canada, Aug. 2-4, 2017

[11] Ji Y F, Peng M J, Lin Q, Yin C P. Wire-driven parallel robot suspension system for SDM in a low-speed wind tunnel. Advances in Mechanical Engineering, 2023, 15(4).

[12] Williams R L. Novel cable‐suspended RoboCrane support. Industrial Robot: An International Journal, 2005, 32(4):326-333.

[13] El-Ghazaly G, Gouttefarde M, Creuze V. Adaptive terminal sliding mode control of a redundantly-actuated cable-driven parallel manipulator: CoGiRo. 2nd International Conference on Cable-Driven Parallel Robots, Duisburg, Germany,2014

[14] Miermeister P, Laechele M, Boss R, Masone C, Schenk C, Tesch J, Kerger M, Teufel H, Pott A, Bulthoff H H, IEEE. The CableRobot simulator large scale motion platform based on cable robot technology. 2016 IEEE/RSJ International Conference on Intelligent Robots and Systems (IROS 2016), Seoul, Korea, Oct. 8-9, 2016

[15] Linner T, Pan W, Hu R, Zhao C, Iturralde K, Taghavi M, Trummer J, Schlandt M, Bock T. A technology management system for the development of single-task construction robots. Construction Innovation, 2020, 20(1):96-111.

[16] Zi B, Wang N, Qian S, Bao K. Design, stiffness analysis and experimental study of a cable-driven parallel 3D printer. Mechanism and Machine Theory, 2019, 132:207-222.

[17] Behzadipour S, Khajepour A. A new cable-based parallel robot with three degrees of freedom. MULTIBODY SYSTEM DYNAMICS, 2005, 13(4):371-383.

[18] Xie G Q, Zhang Z K, Shao Z F, Wang L P. Research on the orientation error of the translational cable-driven parallel robots. Journal of Mechanisms and Robotics-Transactions of the ASME, 2022, 14(3).

[19] Zhang Z K, Shao Z F, Peng F Z, Li H S, Wang L P. Workspace analysis and optimal design of a translational cable-driven parallel robot with passive springs. Journal of Mechanisms and

Robotics-Transactions of the ASME, 2020, 12(5).
[20] Rasheed T, Long P, Caro S. Wrench-feasible workspace of mobile cable-driven parallel robots. Journal of Mechanisms and Robotics-Transactions of the ASME, 2020, 12(3).
[21] Erskine J, Chriette A, Caro S. Wrench analysis of cable-suspended parallel robots actuated by quadrotor unmanned aerial vehicles. Journal of Mechanisms and Robotics-Transactions of the ASME, 2019, 11(2).
[22] Liu Y, Zhang F, Huang P, Zhang X. Analysis, planning and control for cooperative transportation of tethered multi-rotor UAVs. Aerospace Science and Technology, 2021, 113.
[23] Eden J, Lau D, Tan Y, Oetomo D. Available acceleration set for the study of motion capabilities for cable-driven robots. Mechanism and Machine Theory, 2016, 105:320-336.
[24] Finotello R, Grasso T, Rossi G, Terribile A. Computation of kinetostatic performances of robot manipulators with polytopes. IEEE International Conference on Robotics and Automation, Leuven, Belgium, May 16-20, 1998
[25] Garg V, Nokleby S B, Carretero J A. Wrench capability analysis of redundantly actuated spatial parallel manipulators. Mechanism and Machine Theory, 2009, 44(5):1070-1081.
[26] Zibil A, Firmani F, Nokleby S B, Podhorodeski R P. An explicit method for determining the force-moment capabilities of redundantly actuated planar parallel manipulators. Journal of Mechanical Design, 2007, 129(10):1046-1055.
[27] Bosscher P, Riechel A T, Ebert-Uphoff I. Wrench-feasible workspace generation for cable-driven robots. IEEE Transactions on Robotics, 2006, 22(5):890-902.
[28] Bouchard S, Gosselin C, Moore B. On the ability of a cable-driven robot to generate a prescribed set of wrenches. Journal of Mechanisms and Robotics-Transactions of the ASME, 2010, 2(1).
[29] Hussein H, Santos J C, Izard J, Gouttefarde M. Smallest maximum cable tension determination for cable-driven parallel robots. IEEE Transactions on Robotics, 2021, 37(4):1186-1205.
[30] Liu S, Mei J, Wang P, Guo F. Optimal design of a coupling-input cable-driven parallel robot with passive limbs based on force space analysis. Mechanism and Machine Theory, 2023, 184:105296.
[31] Sun G Y, Liu Z, Gao H B, Li N, Ding L, Deng Z Q. Direct method for tension feasible region calculation in multi-redundant cable-driven parallel robots using computational geometry. Mechanism and Machine Theory, 2021, 158.
[32] Chan A, Lau D, Lam S. Wrench and twist capability analysis for cable-driven parallel robots with consideration of the actuator torque-speed relationship. IEEE Transactions on Robotics, 2023, 39(4):3185-3199.
[33] Yin J N, Jiang P, Yao R. Pose optimization of the FAST feed support system based on the new feed cabin mechanism. Science China: Physics, Mechanics & Astronomy, 2023, 66(3):239513.
[34] Althoff M, Stursberg O, Buss M. Computing reachable sets of hybrid systems using a combination of zonotopes and polytopes. Nonlinear Analysis: Hybrid Systems, 2010, 4(2):233-249.
[35] Gouttefarde M, Krut S. Characterization of parallel manipulator available wrench set facets. 12th International Symposium on Advances in Robot Kinematics (ARK 2010), Piran Portoroz, Slovenia, Jun. 27-Jul. 1, 2010
[36] Barber C B, Dobkin D P, Huhdanpaa H T. The Quickhull algorithm for convex hulls. ACM Transactions on Mathematical Software, 1996, 22(4):469-483.
[37] Elizondo D. The linear separability problem: some testing methods. IEEE Transactions on Neural Networks, 2006, 17(2):330-344.
[38] Ziegler G M. Lectures on polytopes. New York: Springer Science+Business Media, 1995.
[39] Billera L J, Bjorner A. Face numbers of polytopes and complexes//Handbook of Discrete and Computational Geometry, Second Edition. 2004:418-441.
[40] Brondsted A. An introduction to convex polytopes. New York: Springer New York, 1983.
[41] Firmani F, Zibil A, Nokleby S B, Podhorodeski R P. Wrench capabilities of planar parallel manipulators. Part I: Wrench polytopes and performance indices. Robotica, 2008, 26(6):791-802.
[42] Imamura A. Horizontal Fixed Attitude Flight of Quad Rotor Helicopter with Tilting Rotor. Journal of Robotics and Mechatronics. 35(2), 2023:317-327.
[43] Pott A. On the Limitations on the lower and upper tensions for cable-driven parallel robots//Advances in Robot Kinematics. Cham: Springer International Publishing, 2014:243-251.

[44] Beaufort scale, Wikipedia. https://en.wikipedia.org/wiki/Beaufort_scale.
[45] Geographic Data Sharing Infrastructure, College of Urban and Environmental Science, Peking University. http://geodata.pku.edu.cn.